nature communications

Article

https://doi.org/10.1038/s41467-025-58421-1

Continuous sensorimotor transformation enhances robustness of neural dynamics to perturbation in macaque motor cortex

Received: 22 May 2024

Accepted: 20 March 2025

Cong Zheng [1,2,3,4], Qifan Wang [1,2,3] & He Cui [1,2,3,4]

Neural activity in the motor cortex evolves dynamically to prepare and generate movement. Here, we investigate how motor cortical dynamics adapt to dynamic environments and whether these adaptations influence robustness against disruptions. We apply intracortical microstimulation (ICMS) in the motor cortex of monkeys performing delayed center-out reaches to either a static target (static) or a rotating target (moving) that required interception. While ICMS prolongs reaction times (RTs) in the static condition, it does not increase RTs in the moving condition, correlating with faster recovery of neural population activity post-perturbation. Neural dynamics suggests that the moving condition involves ongoing sensorimotor transformations during the delay period, whereas motor planning in the static condition is completed shortly. A neural network model shows that continuous feedback input rapidly corrects perturbation-induced errors in the moving condition. We conclude that continuous sensorimotor transformations enhance the motor cortex's resilience to perturbations, facilitating timely movement execution.

As Albert Einstein once said: Life is like riding a bicycle. To keep your balance, you must keep moving[1]. This metaphor illustrates the principle that motion, rather than remaining still, enables stability and resilience in the face of external disturbances. This is true not only because actions, or movements, are the only valid ways we connect to the world[2], but also because the neural population functions as a dynamical system that continuously evolves over time, performing computations to generate movement[3–6]. In such a process, driven by intrinsic motor cortical dynamics and inputs from other brain regions, preparatory activity sets the neural state into an optimal initial condition, seeding the near-autonomous rotational dynamics of cortical states during movement[7–10]. Preparatory activity is acknowledged as a key link in the causal chain that generates voluntary movement, yet several paradoxes remain unsolved. Disrupting the preparatory states with intracortical microstimulation (ICMS) leads to an increase in reaction times (RTs), supporting the hypothesis that movement preparation is a time-consuming optimization process and that movement is delayed if errors are still present[11]. However, subsequent studies suggest that the preparatory activity could be bypassed or occur unexpectedly rapidly if needed, raising questions about the nature of the delay-period activity[12,13].

Multiple studies have revealed conserved preparatory activity across contexts[13,14], echoing experimental findings that ICMS induces similarly stereotyped RT responses regardless of context[15]. While the commonality of preparatory activity is recognized, the role of differences in neural dynamics in adapting to distinct contexts, particularly dynamic environments, remains unclear. Interception is a context of reaching that requires substantial interaction with a dynamically changing environment. Successful interception demands ongoing predictions and updates of sensorimotor states[16–22]. Recently, we showed that target motion significantly affects neural activity in the macaque motor cortex during interception preparation[23]. The continuous sensorimotor transformation involves multiple brain regions, especially the posterior parietal cortex[24–26], which continuously sends external inputs to motor cortex[23,27–31]. Although this dynamic context appears to differ from context of reaches to static targets, direct

---

[1] Institute of Neuroscience, Center for Excellence in Brain Science and Intelligence Technology, Chinese Academy of Sciences, Shanghai 200031, China. [2] Beijing Institute for Brain Research, Chinese Academy of Medical Sciences & Peking Union Medical College, Beijing 102206, China. [3] Chinese Institute for Brain Research, Beijing 102206, China. [4] These authors jointly supervised this work: Cong Zheng, He Cui. e-mail: zhengcong26@live.com; hecui@cibr.ac.cn

evidence elucidating whether preparatory dynamics differ between these contexts and how such differences contribute to computations is still lacking.

Recent studies highlight the importance of incorporating external inputs to fully understand intrinsic neural dynamics[32–34]. Utilizing an innovative perturbation design, researchers have dissected the roles of local dynamics and external inputs in cortical pattern generation, demonstrating that motor generation is driven by inputs from motor thalamus[33]. Modeling work further indicates that optimal feedback inputs are critical for optimizing motor cortical neural states to enable rapid motor preparation[35], and that optimal control inputs can autonomously seed preparatory states for movement generation[36]. Given the sensorimotor information that feeds into the motor cortex during interception, it is intriguing to explore whether and how these inputs shape neural dynamics.

The present study addressed the important question of whether distinct preparatory dynamics in the motor cortex generate different degrees of robustness to perturbations of these dynamics. We trained two monkeys to perform delayed center-out reaches toward either a static target (static condition) or intercepting reaches toward a rotating target (moving condition). The monkeys showed similar reach trajectories in both conditions. However, ICMS during the late delay period selectively prolonged RTs in the static, but not in the moving condition. Neural states post-ICMS diverged less from intact states in the moving condition, which was associated with a more rapid recovery rate. For moving targets, target or reach direction representations adapted with motion, remaining stable throughout the delay period. Using a neural network model, we illustrated that continuous feedback inputs from other brain regions quickly corrected perturbation-induced errors in the moving condition. These findings reveal differential ICMS effects on neural dynamics and highlight the role of continuous sensorimotor transformation in resilience to unexpected perturbations.

Results

Reach kinematics in the static and moving conditions

We trained two monkeys (G and L) to perform delayed center-out reaches either to a static target (static condition) or a rotating target that needed to be intercepted (moving condition)[16]. Interception requires predicting future reach directions based on a model of target motion and one's kinematics (Fig. 1a). In a typical session, target velocities were either 0°/s (static) or clockwise 120°/s (−120°/s, moving), with delay periods of 200 ms (short, s) or 900 ms (long, l) (Fig. 1b). The initial locations for the moving targets were designed to encourage reaches towards four evenly distributed directions. These designed trials were interleaved with trials featuring random initial target locations, comprising 40–60% of the total trials to maintain randomness and prevent the prediction of reach direction (Fig. 1c). We required the reach endpoints to fall within 2.8 cm of the targets, a criterion that both monkeys met post-training. Endpoint distributions were direction-specific, consistently lagging behind or landing ahead of the target in both target velocity conditions, with minimal variance, indicating habituated reach strategies (Fig. 1d).

Reach trajectories were comparable between the static and moving conditions. When aligned to the same directions, similar curving patterns emerged in both conditions across the four reach directions (Fig, 1e). Analyses of launching angles revealed minor differences between the static and moving conditions, suggesting that the curvature of these trajectories may be influenced by gravitational or biomechanical constraints, as this pattern was also observed in the static condition (Supplementary Fig. 1b). Hand peak speeds were generally higher in the moving condition, though the difference varied by reach directions (Fig. 1f). Reaction times (RTs) were typically longer in the moving condition (Fig. 1g). A longer delay period decreased RTs for the moving condition in monkey G and for the static condition in monkey L, indicating that extended preparation time facilitates adequate motor planning, consistent with previous studies[37–39]. Some trials showed RTs below 150 ms, which is expected, as moving targets can elicit fast, reactive interceptive movements[13,40,41]. Further analyses indicate that 35.3% (short delay) and 52.2% (long delay) of trials with RTs below 150 ms were from the designed conditions for monkey G, while these proportions were 42.1% (short delay) and 52.9% (long delay) for monkey L, suggesting that shorter RTs reflect biological variability rather than anticipation of go cue (GO). Overall, with sufficient preparation time, monkeys exhibited well-prepared reaches during interception, suggesting they relied on predictions of future reach directions rather than targeting the instantaneous target position; otherwise, the reach trajectory would have shown significant curved[22].

Perturbation delays initiation of reaches directed at the static but not the moving targets

Experimental perturbations, such as intracortical microstimulation (ICMS), can provide insights into neural dynamics[11,15,42,43]. Following the methodology established by Churchland and Shenoy[11], we applied subthreshold ICMS (100 ms at 300 Hz) to either primary motor cortex (M1) or dorsal premotor cortex (PMd) using a single electrode, while simultaneously recording nearby neural activity with a 64-channel linear probe (Fig. 2a). ICMS amplitudes were set 5–10 μA below threshold, determined by gradually increasing the stimulation until a muscle twitch or movement occurred, then reducing the amplitude until no movement was detected. Electromyography (EMG) analyses indicated that ICMS rarely elicited muscle activity (Supplementary Fig. 2a). Since critical preparatory neural dynamics primarily occur during the late delay period, ICMS was timed around the go cue (PreGO, from GO − 100 ms to GO) or just before movement onset (PreMO, from GO to GO + 150 ms) (Fig. 2b). Trials with stimulation (stimulated, ST) and without stimulation (non-stimulated, NS) were randomly interleaved. In the following analyses, we primarily focused on the effects of ICMS in the long-delay condition, although ICMS was also applied in the short-delay condition (Supplementary Figs. 3 and 4).

The impact of ICMS on reach accuracy or movement kinematics, such as hand speed, was minimal (Fig. 2c, Supplementary Fig. 3, 4). However, ICMS produced contrasting effects on RTs: it prolonged RTs in the static condition while shortening RTs in the moving condition (Fig. 2d). We calculated changes in RTs ($\Delta RT = RT_{ST} - RT_{\text{matched NS}}$) and found that PreGO ICMS prolonged RTs in the static condition by 13.3 ms (95% CI: [7.5, 18.2]) for monkey G. PreMO ICMS increased RTs by 10.3 ms (95% CI: [3.6, 16.3]) for monkey G and 15.0 ms (95% CI: [8.0, 23.1]) for monkey L. These findings align with previous studies[11,42]. For monkey L, significant RT prolongation was observed only in the PreMO ICMS condition. Given monkey L's generally longer RTs (Fig. 1g), PreMO ICMS timing may be closer to the critical preparatory epoch just before movement onset. In contrast, PreGO ICMS shortened RTs in the moving condition by 8.2 ms (95% CI: [−16.3, 1.3]) for monkey G and 8.2 ms (95% CI: [−14.6, −1.5]) for monkey L. The earlier timing of PreGO ICMS likely allowed for a greater reduction in RTs compared to PreMO ICMS. We also examined the average ΔRT across individual sessions, and the distributions of ΔRT confirmed that most sessions experienced increased RTs in the static condition and decreased RTs in the moving condition after ICMS (Fig. 2e).

The ICMS effect on RTs was found to be location-dependent (Fig. 2f, g). Specifically, stimulation of more anterior sites, such as PMd, resulted in a more pronounced RT-prolonging effect in the static condition, consistent with previous studies suggesting a close correlation between PMd activity and motor preparation[11,44]. Although there was a trend indicating that the RT-shortening effect in the moving condition was more evident in anterior areas, the relationship between antero-posterior location and RT differences was not statistically

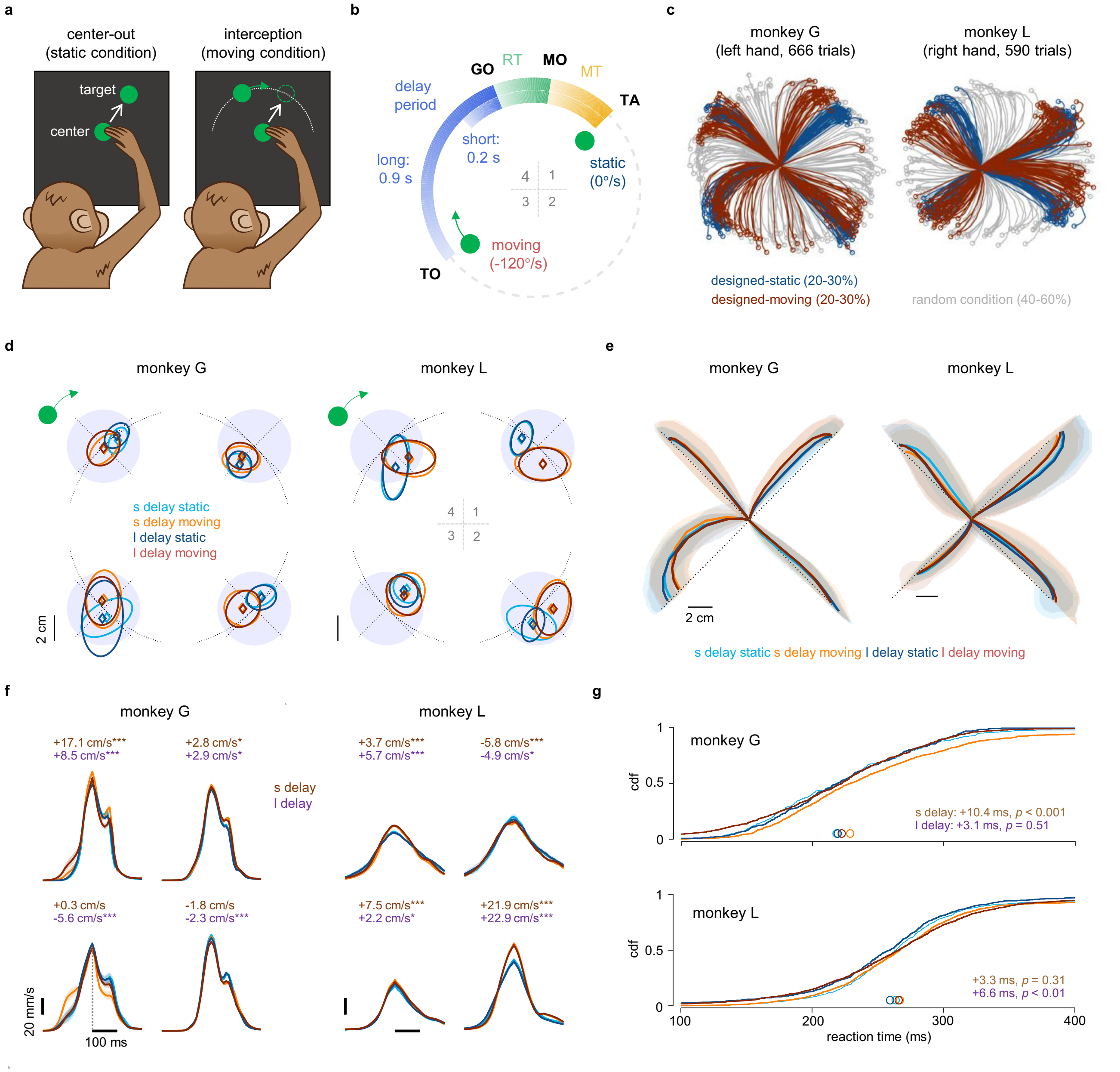

Fig. 1 | Reach kinematics in the static and moving conditions. a Task description. Monkeys performed two types of reach tasks: reaching for a static target or intercepting a moving target. **b** Task structure. Target onset (TO) is followed by a delay of either 200 ms (short, s) or 900 ms (long, l). The dimmed center green dot indicates go cue. Movement onset (MO) and target acquisition (TA) delineate reaction times (RTs) and movement times (MTs). **c** Reach trajectories from example sessions. The designed static and moving conditions share a similar reach direction for statistical comparison, while the random condition features random initial target locations to avoid predictability. **d** Reach endpoints relative to target locations, represented as mean ± 95% confidence interval (CI). Subplots correspond to four reach directions. Dotted black lines indicate tangential and radial directions relative to target location. Purple shading denotes the error tolerance range. See Supplementary Table 1 for the number of trials in (**d**–**g**). Annotations are consistent across (**d**–**g**). **e** Reach trajectories aligned to the corresponding directions (mean ± 68% CI). **f** Hand speed profiles aligned to the peak speed (mean ± 95% CI). Differences in peak speed ($v_{moving} - v_{static}$) are noted ($^{*}p < 0.05$, $^{***}p < 0.001$, two-sided Wilcoxon rank sum test). **g** Empirical cumulative distribution function (CDF) for RTs. Colored circles indicate the median RT. The differences in RT ($RT_{moving} - RT_{static}$) are noted (two-sided Wilcoxon rank sum test). Source data are provided as a Source Data file.

significant. This suggests that, while the RT-shortening effect in the moving condition may be associated with preparatory activity, its underlying mechanisms could differ from those of RT-prolonging effect observed in the static condition. In addition, no significant correlations were found between ΔRT and ICMS amplitudes (Supplementary Fig. 2c), indicating that the location-dependent effect is unlikely to be due to higher ICMS thresholds in PMd (Supplementary Fig. 2b). To further validate these findings, we conducted a series of control analyses to account for potential impacts of calculation method of ΔRT, trial order, and condition randomness (Supplementary Figs. 5–7)

Faster recovery from perturbed states in the moving condition

To investigate the mechanisms underlying ICMS-induced RT changes, we analyzed the neural activity recorded concurrently with ICMS. Due to potential ICMS artifacts, we restricted our analyses to periods outside the ICMS window, setting neural data within this window to zero during computation and excluding it from displayed results. Post-

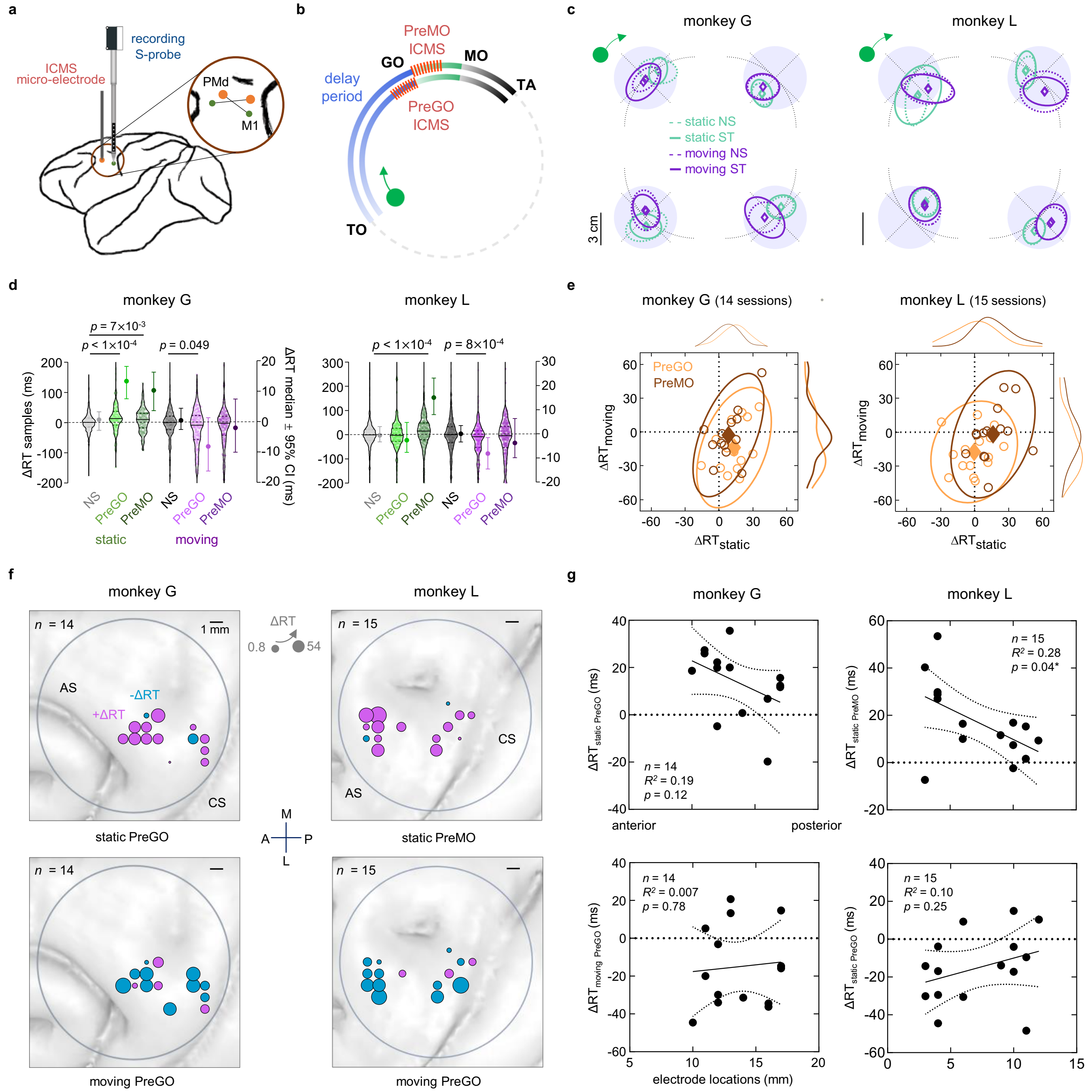

Fig. 2 | ICMS increases reaction times in the static condition but not in the moving condition. a Microstimulation and recording setup. Inset illustrates the electrode pairs used for stimulation (orange) and recording (green) in either PMd or M1. Also see Supplementary Fig. 2d. **b** Timing of microstimulation in the long-delay condition. ICMS is delivered at either PreGO (100–0 ms before GO) or PreMO (0–150 ms after GO). The timing for the short-delay condition remains consistent with this. **c** Reach endpoints relative to target locations after ICMS (mean ± 95% CI). Annotations are consistent with those in Fig. 1d. See Supplementary Table 1 for the number of trials. **d** Changes in RT ($\Delta RT = RT_{ST} - RT_{\text{matched NS}}$) averaged across reach directions in the long-delay condition. Individual trial distributions are visualized as violin plots with sample points (left y-axis). Solid lines indicate the median ΔRT, and dashed lines represent the 25th and 75th percentiles. Dots with error bars representing median ΔRT ± 95% CI, shown separately for clarity (right y-axis). Statistical comparisons were performed using two-sided Wilcoxon rank-sum test, with *p*-values indicated ($n = 338, 154, 166, 507, 158, 167$ trials for monkey G; $n = 574, 262, 277, 873, 258, 274$ trials for monkey L). **e** Individual session ΔRTs. Circles indicate median ΔRT of individual sessions, accompanied by marginal histograms. Filled diamonds and ellipses indicate means and 95% CI. **f** Location-dependent ICMS effect on RTs. Dot size represents the magnitude of ΔRT, with the minimum and maximum sizes indicated in the inset. Colors denote the sign of ΔRT (cyan for negative, purple for positive). Number of sessions are denoted. **g** ΔRT as a function of anterior-posterior location. Electrode locations range from 0 (anterior, PMd) to 20 (posterior, M1). Dotted curves indicate the 95% CI for a linear fit. Goodness of fit (R^2) is reported. The *p*-value testing the null hypothesis that the overall slope is zero was obtained using an *F* test. Number of sessions are denoted. Source data are provided as a Source Data file.

ICMS single-unit responses predominantly exhibited either inhibitory or excitatory patterns (Fig. 3a). Previous studies indicate that high-amplitude ICMS typically lead to longer inhibition periods, with durations increasing exponentially beyond a 40 μA threshold[45]. In our sessions, the mean ICMS amplitudes were 67.5 ± 22.1 μA for monkey G and 34.7 ± 11.4 μA for monkey L, which might explain the higher proportion of inhibitory responses observed. We also examined the impact of proximity to stimulating sites on ICMS responses, finding a

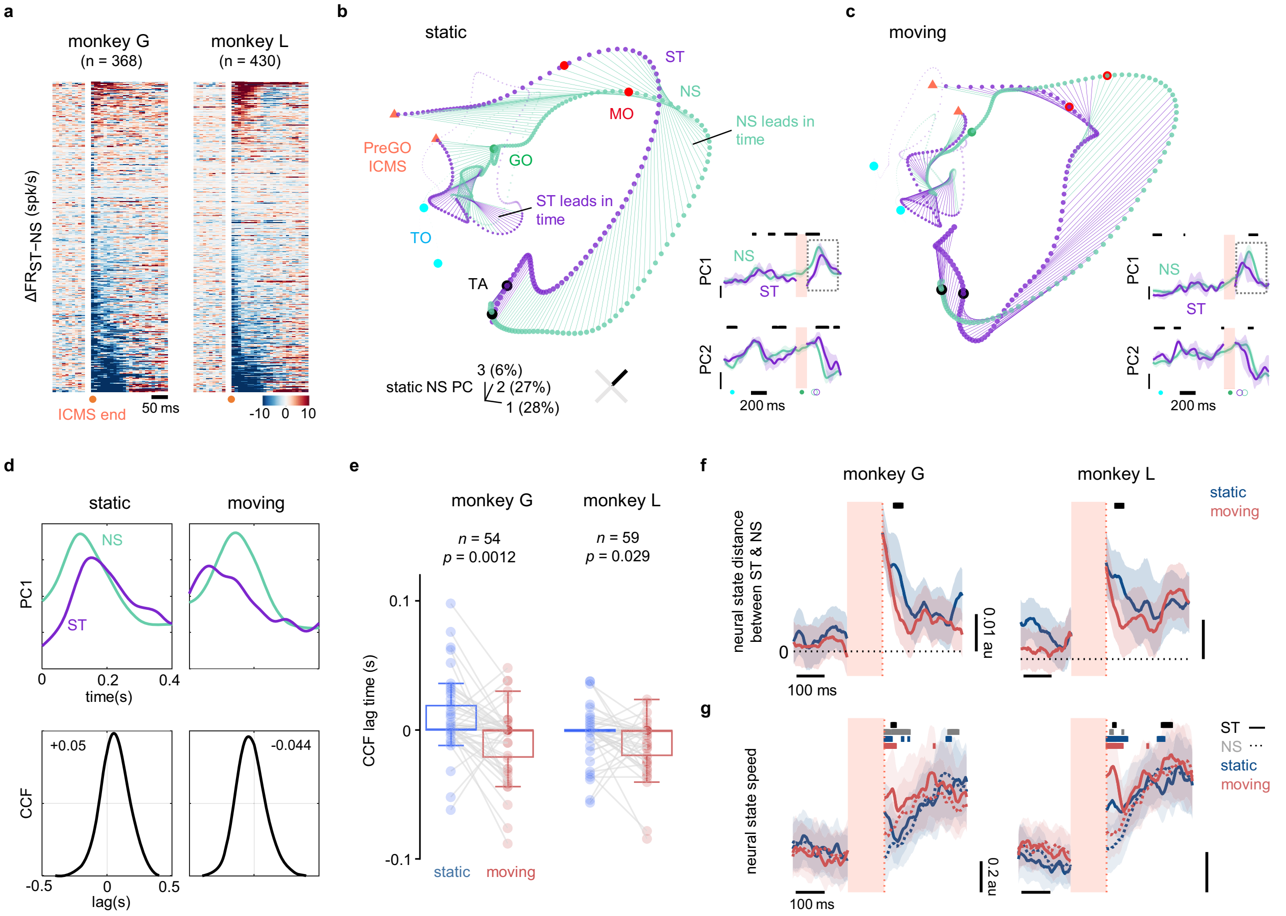

Fig. 3 | Faster recovery from perturbed states in the moving condition. **a** Neuronal response post-ICMS. Changes in firing rates ($\Delta FR = FR_{ST} - FR_{matched\ NS}$) aligned to end of ICMS, with ICMS-period activity removed. Units are sorted by ΔFR within a 100 ms post-ICMS window. **b, c** Neural trajectories and the first two principal components (PCs, mean ± 95% CI) for a representative static (**b**) or moving condition (**c**) in the same state space. The orange triangles indicate the start and end of ICMS, with ICMS-period activity omitted. Colored lines connecting NS and ST conditions at each time point indicate which condition is relatively ahead along the trajectory. The black lines at the top of the insets represent time intervals during which significant differences between the two conditions are observed ($p < 0.05$, two-sided Wilcoxon rank sum test). **d** Example cross-correlation function (CCF) for PC1. Top: PC1 of the time epoch shown in (**b**, **c**) (dashed box). Bottom: CCF between NS and ST conditions. The lag time, where the CCF peaks, is noted in seconds. **e** Pooled CCF lag times across reach directions and sessions. Bounds of box represent the interquartile range (IQR), with bold line for the median. The whiskers extend to the smallest and largest values within 1.5 × IQR from Q1 and Q3. Statistical comparisons were performed using the two-sided Wilcoxon signed rank test, with *p*-values indicated. Number of samples are denoted. **f** Neural state distance between NS and ST conditions (mean ± 95% CI). Data are aligned to end of ICMS and averaged across reach directions and sessions (monkey G: $n = 13 \times 4 = 52$ samples; monkey L: $n = 15 \times 4 = 60$ samples). Orange shading marks the ICMS duration. Black lines indicate time intervals with significant differences ($p < 0.05$, two-sided Wilcoxon rank sum test). **g** Neural state speed (mean ± 95% CI). Data are aligned to end of ICMS and averaged (monkey G: $n = 7 \times 4 = 28$ samples; monkey L: $n = 12 \times 4 = 48$ samples). Colored lines above indicate time intervals with significant differences ($p < 0.05$, two-sided Wilcoxon rank sum test) between the static and moving condition at ST (black) and NS (gray), as well as differences between NS and ST in the static (blue) and the moving condition (red). Other annotations follow panel (**f**). Source data are provided as a Source Data file.

modest but significant positive correlation in monkey L's data (Supplementary Fig. 2e), suggesting that units located farther from the stimulation site exhibit higher rates of excitation, consistent with previous findings[46].

We next applied principal component analysis (PCA) to analyze neural population activity. A 3D subspace, which explained over 60% of the variance, was constructed using condition-averaged NS trials from the static condition, providing a basis for projecting into other conditions. Neural trajectories for NS and ST trials initially evolved in parallel but diverged after ICMS, with ST trajectories lagging in the static condition and leading in the moving condition (Fig. 3b, c; Supplementary Figs. 8 and 9). Given the established association between the advancement of neural states at GO and RTs[47,48], we performed a cross-correlation function (CCF) on PC1 to estimate the lag time between NS and ST conditions (Fig. 3d). Results indicated that the average lag times were positive in the static condition but negative in the moving condition, corresponding with the observed RT changes post-ICMS (Fig. 3e).

To further examine the differences between NS and ST trials, we computed their neural state distance using an unbiased estimation approach[49]. Results indicated a smaller neural distance after ICMS in the moving condition compared with static condition, suggesting that ICMS induced less deviations from intact states in the moving condition (Fig. 3f). We further analyzed the evolving speed of neural states and found that post-ICMS neural state speeds were higher in the moving condition than in the static condition, although neural speed in the static condition also increased by the end of ICMS (Fig. 3g). This finding suggests that the smaller neural distances in the moving condition might result from quicker recovery from ICMS-induced deviations. Overall, the prolonged RTs observed in the static condition post-ICMS align with a lag in neural states, likely due to deviations that require additional time to recover. In contrast, neural states in the

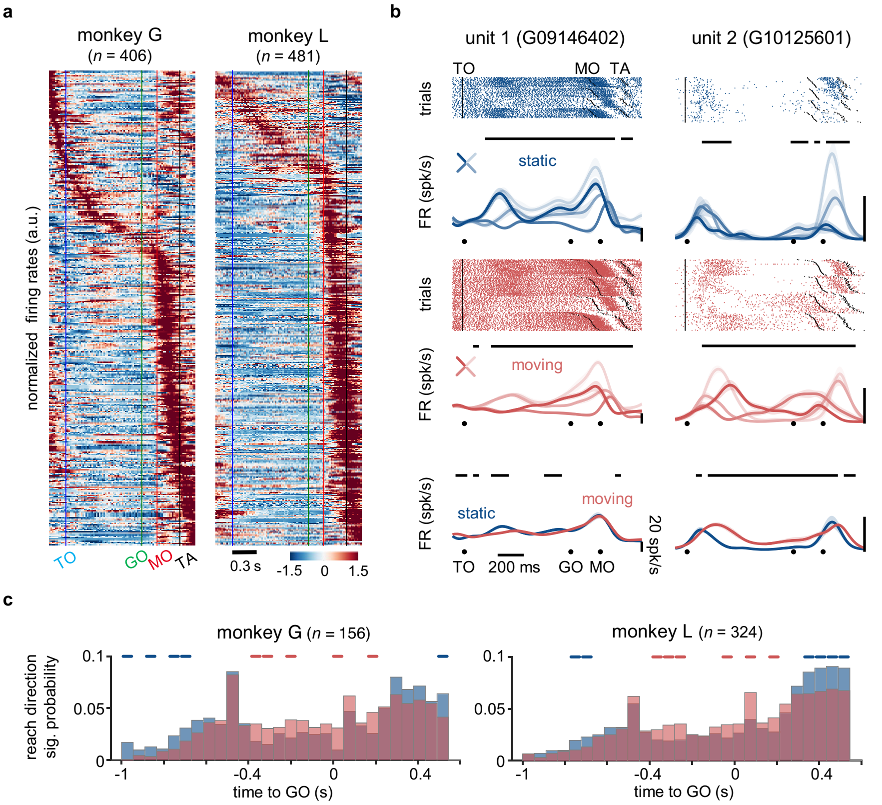

Fig. 4 | The static and moving conditions differ at the single-unit level. **a** Heatmap of normalized firing rates for single units. Neural activity in the long-delay condition is aligned to GO, with units sorted by the time of peak firing rates. **b** Example neural spike rasters and peri-event time histograms (PETHs; mean ± SEM). Black lines above indicate time intervals with significant difference ($p < 0.05$) based on Kruskal–Wallis test (top and middle) and two-sided Wilcoxon rank sum test (bottom). **c** Normalized histogram showing the distribution of time bins summed across units where firing rates differ significantly across reach directions (Kruskal–Wallis test, $p < 0.05$). A significant right-tail Fisher's exact test ($p < 0.05$, blue lines above) indicated a greater count in the static condition compared to the moving condition, while the significant left-tail test ($p < 0.05$, red lines above) suggested a significantly smaller count in static condition. Source data are provided as a Source Data file.

moving condition are less disrupted and even exhibit accelerated dynamics, likely because the faster-evolving speed of neural states reduces recovery time.

It was proposed that ICMS-induced changes in RTs can be interpreted within a framework where the brain delays movement initiation until preparatory errors are minimized, with larger errors leading to longer RTs[11]. Deviations in neural states following ICMS may represent these preparatory errors, and recovery from such states would correspond to error resolution. The faster these errors are corrected, the quicker motor preparation completes, enabling timely movement execution. Our findings support this framework and raise an important question: do the differences in ICMS responses arise from intrinsic variations in preparatory neural dynamics between the static and moving conditions, despite their similar reach kinematics?

The static and moving conditions differ at the single-unit level

To explore potential differences in neural dynamics between the static and moving conditions, we firstly examined single-neuron activity. Most sorted single units showed activations during either the delay period or movement (Fig. 4a). However, the proportion of neurons exhibiting pronounced pre-movement or preparatory responses was relatively lower in monkey L, likely due to sampling bias. While single-neuron activity exhibited reach-direction tunings, this tuning was more complex and sustained in the moving condition (Fig. 4b). For instance, unit 1 maintained consistent directional tuning throughout the delay period in the static condition, whereas its tuning varied in the moving condition. Unit 2 showed significantly higher firing rates in the moving condition. To quantify these findings, we summed the number of time bins with significant differences in firing rates across reach directions for all units. The results showed the static condition had a relatively larger proportion of directional tuning around TO and during movement, while the moving condition exhibited a steadily increased directional tuning during late delay (Fig. 4c). This suggests that the representation of sensorimotor information is a gradual process in the moving condition, whereas in static condition, this process is rapidly completed after TO. Further analysis of the preferred directions (PDs) of individual neurons confirmed that most neurons exhibited stably, varying tunings in the moving condition, whereas directional tuning was most stable around TO and after GO in the static condition (Supplementary Figs. 10 and 11).

Continuous sensorimotor transformation during preparation in the moving condition

Given the intriguing single-neuron activity, we further explored the neural population dynamics. Using PCA to visualize low-dimensional neural population activity, we observed that the primary difference in neural trajectories between the static and moving conditions mainly occurred during the late delay period (Fig. 5a). Although both conditions evolved roughly in parallel, the neural trajectories in the static condition twisted significantly around GO, whereas those in the moving condition remained relatively straight. This finding was quantified and confirmed across sessions, indicating that neural states maintained in the static condition, while they continued to evolve in the moving condition (Supplementary Fig. 12).

Next, we performed targeted dimensionality reduction (TDR) on the condition-averaged neural activity to identify a low-dimensional

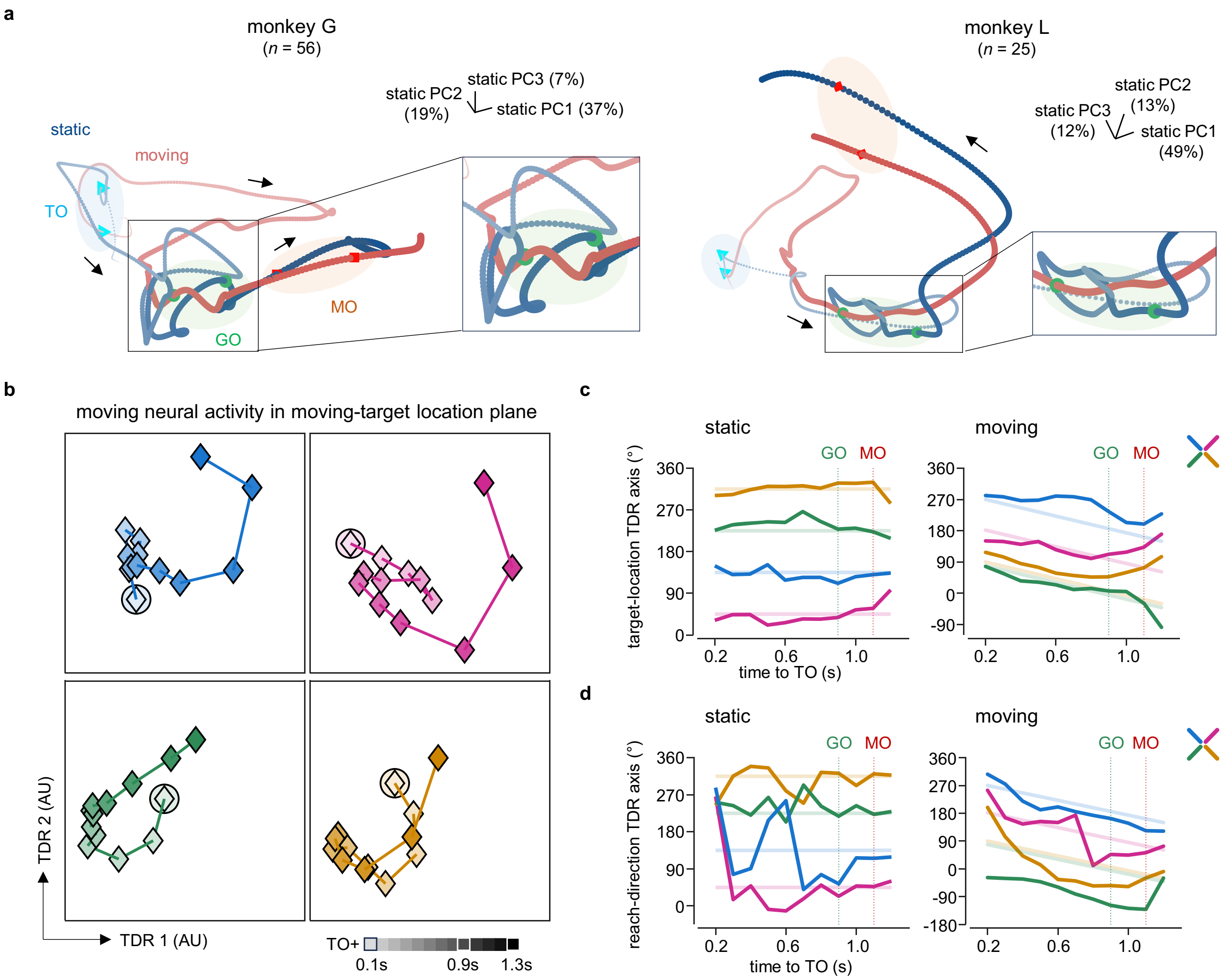

Fig. 5 | Continuous sensorimotor transformation during preparation in the moving condition. a Neural trajectories for one example reach direction in the subspace constructed from the static condition. Colored filled circles mark events, and insets provide enlarged views of neural trajectories around GO. **b** Neural states over time in target-location TDR subspace for the moving condition, constructed from neural activity at TO + 0.1 s (large filled circles). Neural states are shown for each reach direction separately. Data are averaged across seven sessions from monkey G, with 181 neurons. **c** Temporal changes in neural states relative to TO + 0.1 s within the static (left) and moving (right) target-location TDR subspaces. Neural states in the moving condition evolved clockwise, while those in the static condition remained stable after TO. Data are the same as in (**b**). **d** Time course of absolute change in neural state position in the static (left) and moving (right) reach-direction TDR subspace. Neural states in both conditions converged to similar relative positions by MO. Data are the same as in (**b**). Source data are provided as a Source Data file.

subspace that captures variance associated with target location or reach direction[50–52]. We constructed the target location subspace separately for the static and moving conditions using neural activity 100 ms after TO. In the moving condition, the neural states rotated clockwise around the neural state at TO + 100 ms, whereas neural states in the static condition remained largely unchanged (Fig. 5b, c). This suggests the presence of neurons responsive to target motion. In the reach-direction plane, constructed using neural activity 100 ms before MO, the neural states in the moving condition also rotated clockwise, gradually evolving towards the states near MO. In contrast, neural states in the static condition displayed a more stable representation of motor intention around TO and after GO (Fig. 5d; Supplementary Fig. 13). We also performed linear decoding of target location and reach direction, which supports these findings and suggests that, in the static condition, the motor plan is formed rapidly after TO and then maintained during the late delay period. In contrast, the moving condition experiences continuous sensorimotor transformation throughout the entire delay period (Supplementary Fig. 14).

Cortical neural dynamics can be shaped by external inputs. Preparatory activity in premotor cortex remains resilient under unilateral silencing, likely due to corrective input from the opposite hemisphere[53]. Motor cortex receives strong, time-varying inputs from the thalamus for movement generation[33], and these inputs may help resolve preparatory motor errors, thereby resisting perturbation[35]. Given that continuous sensorimotor transformations involve a constant influx of inputs to the motor cortex[54–56], we next built a model to illustrate how differences in preparation-related external inputs could potentially lead to divergent neural dynamics and ICMS responses.

Input-driven model simulates ICMS effect on RTs

To illustrate our hypothesis, we utilized the neural network model developed by Kao et al., which employs optimal feedback control for motor preparation[35]. During a reaching task, target information is received and generates a motor intention, i.e., the optimal states $\mathbf{x}^*$ (fixed points corresponding to future reach directions). Based on $\mathbf{x}^*$ and the current states of motor cortex, control input $\mathbf{u}$ from recurrently connected brain regions drives the circuit to the appropriate state, guiding the arm toward the desired reach (Fig. 6a). This network consists of 100 excitatory (E) and 100 inhibitory (I) neurons, with a

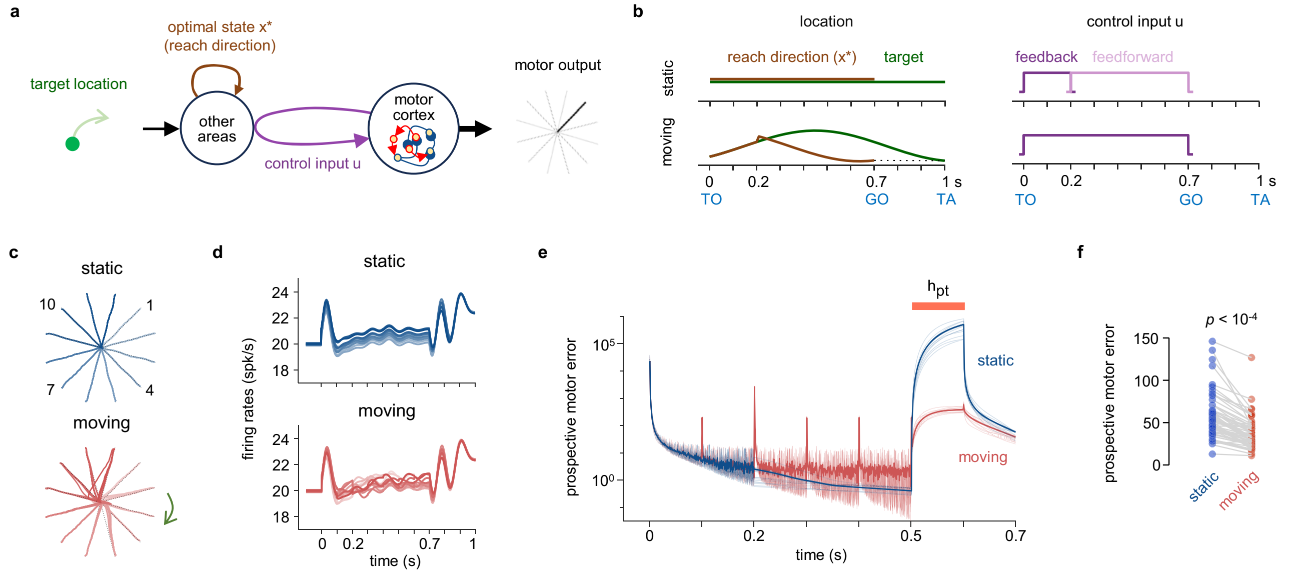

Fig. 6 | Input-driven network model reproduces ICMS effect on RTs. a Diagram of the neural network model. During goal-directed movement, target information is translated into motor intentions (optimal state x*) by upstream areas. Control input u from recurrently connected areas drives motor cortex activity x (with balanced excitatory-inhibitory connectivity) towards an optimal subspace during preparation, with initial states converted to motor outputs (hand positions). **b** Illustration of optimal states and inputs. In the static condition, the optimal state is fixed, while in the moving condition, it is continuously adjusted to lead the target. Control input u in the static condition is feedback-driven initially, and then switches to feedforward control, while remaining feedback-driven in the moving condition. **c** Reach trajectories generated by the model. Dashed black lines indicate desired movement paths. Ten trials with varying initial values are shown for each reach direction. **d** Example PETH for a model unit (#197). Firing rates (mean ± 95% CI) across reach directions are averaged over 10 repetitions with varied initial states and color-coded as in (**c**). Data before time 0 are extended to clarify initial values. **e** Prospective motor error in perturbed condition. Perturbation input h_{pt} (orange bar) with amplitude 50 (a.u.) is applied 200 ms before MO. Thick lines show the mean prospective motor error across 12 directions with 10 initial values. Thin lines show 10 randomly selected examples. **f** Prospective motor error at MO under perturbation (20 repetitions). Perturbation details match those in (**e**). Statistical significance was assessed using the two-sided Wilcoxon signed rank test, with p-value indicated.

fixed connectivity matrix **W** that maintains E/I balance[57,58]:

$$\tau \frac{dx}{dt} = -\mathbf{x}(t) + \mathbf{W}\phi[\mathbf{x}(t)] + \bar{\mathbf{h}} + \mathbf{h}(t) + \mathbf{u}(t) \tag{1}$$

$$\mathbf{y}(t) = \mathbf{C}\phi[\mathbf{x}(t)] \tag{2}$$

where $\bar{\mathbf{h}}$ represents baseline neural activity, $\mathbf{h}(t)$ is an α-shaped input applied during movement, and $\mathbf{u}(t)$ is the external input, active only during the preparation period. The function $\phi(\mathbf{x}) = \max(\mathbf{x}, 0)$ converts internal activations into hand position $\mathbf{y}(t)$. For a delayed reach task with twelve targets, a 700-ms delay, and 300-ms movement time, we optimized x^* and readout matrix $\boldsymbol{C} \in \mathrm{R}^{2\times N}$ by minimizing a loss function (see section "Method").

We adapted the model for our task with two key assumptions (Fig. 6b): (1) Desired optimal states dynamics. In the moving condition, $\mathbf{x}^*$ updates sequentially between adjacent optimal states to simulate continuous sensorimotor transformations (Supplementary Fig. 15). In the static condition, $\mathbf{x}^*$ remains constant. (2) Input control strategies. Optimal feedback control (using Linear Quadratic Regulator, LQR) derives $\mathbf{u}(t) = \mathbf{u}^* + K\boldsymbol{\delta}\mathbf{x}(t)$, where $\boldsymbol{\delta}\mathbf{x}(t)$ is the momentary deviation, $\mathbf{u}^*$ is the reach-specific stationary external input, and K is the optimal gain matrix. Naive feedforward control, where $\mathbf{u}(t) = \mathbf{u}^*$, was dismissed in the original study due to slow network stabilization[35]. However, this strategy effectively maintains a desired state, as observed in the late delay period of the static condition. Thus, we switched from feedback to feedforward control 200 ms after TO in the static condition. In the moving condition, feedback control remains active throughout preparation.

Our model generated accurate hand reach trajectories (Fig. 6c), with units showing stable directional tuning in the static condition and complex firing patterns in the moving condition (Fig. 6d). We applied a 100-ms perturbation $\mathbf{h}_{\mathbf{pt}}$ 200 ms before MO to half of the network's units. Prospective motor error estimates the potential movement error if movement initiation occurs from the current neural state[35]. As expected, perturbations led to higher prospective motor errors in the static condition compared to the moving condition (Fig. 6e, f). Consistently, the additional time required for errors to drop below motor acceptable threshold ($R^2 > 0.9$) was longer in the static condition (Supplementary Fig. 16). Overall, this model suggests that continuous external input to motor cortex could help resist perturbation-induced RT prolongation by efficiently reducing errors.

A plausible explanation for the ICMS-induced acceleration effect in the moving condition

An open question in our study is the PreGO ICMS-induced RT-shortening effect observed in the moving condition. Unlike the RT-prolonging effect in the static condition, this RT reduction does not follow the expected antero-posterior location relationship, suggesting a different underlying mechanism (Fig. 2f, g). Since this reduction in RT occurred without sacrificing reach accuracy, we suspect that it may reflect a voluntary decision rather than a passive response. To explore this, we analyzed eye movements and found that, in the delayed interception task, the monkeys faced a trade-off between responding promptly to GO and accurately tracking the target. PreGO ICMS, applied just before GO, may serve as an implicit cue that facilitates the recognition of visual GO, thereby shortening RTs during interception.

Before GO, the monkey's gaze typically fixated near the center. After GO, the monkey made a saccade followed by smooth pursuit toward the target (Fig. 7a). While eye movements lag behind the instantaneous location of the moving target[16], they still provide valuable information about the target[59–61]. Notably, onset of eye movements occurred earlier than that of hand movements in the moving

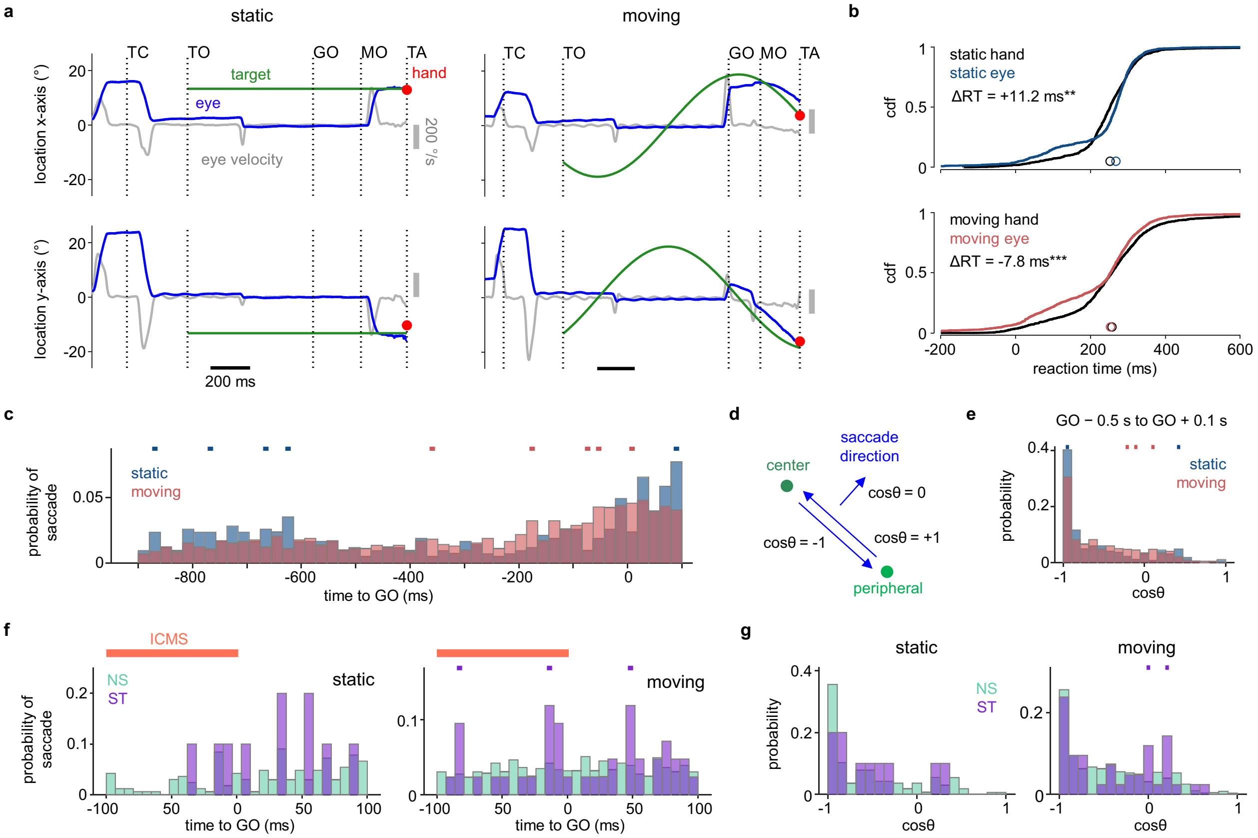

Fig. 7 | A plausible explanation for the ICMS-induced acceleration effect in the moving condition. **a** Eye and target positions, along with eye speed, in a representative trial of the static and moving conditions. The red dot indicates hand touch positions. **b** Empirical cumulative distribution functions (CDFs) of RTs for eye and hand movements in the static ($n = 1927$ trials) and moving ($n = 2486$ trials) condition. RT differences ($\Delta RT = RT_{eye} - RT_{hand}$) were indicated ($^{**}p < 0.01$, $^{***}p < 0.001$, two-sided Wilcoxon rank sum test). **c** Probability of saccade was compared between the static ($n = 755$ trials) and moving conditions ($n = 2588$ trials). A significant right-tail Fisher's exact test ($p < 0.05$, blue lines above) indicated a greater probability in the static condition compared to the moving condition, while the significant left-tail test ($p < 0.05$, red lines above) suggested a smaller probability in static condition. The same annotations and statistical tests apply to panels (**e, f, g**). **d** Schematic illustrating how the cosθ metric indicates saccade direction. **e** Distributions of cosθ for saccades in representative epochs shown in (**c**). **f** Probability of saccade compared between NS and ST trials in the static (NS $n = 391$ trials, ST $n = 76$ trials) and moving (NS $n = 971$ trials, ST $n = 138$ trials) condition, with a target velocity of ±120°/s. The orange line marks ICMS timing (GO − 100ms to GO). **g** Distributions of cosθ for saccades in (**f**). ST trials in the moving condition showed a higher proportion of saccade directed away from target.

condition, but not in the static condition (Fig. 7b). The probability of saccades was also higher during the late delay period in the moving condition (Fig. 7c), mirroring the distribution of significant directional tunings in neural activity (Fig. 4c). To determine the saccade direction, we calculated cosθ, the cosine of angle between the saccade direction and the direction toward the center. (Fig. 7d). Most cos*θ* were around −1, indicating that these saccades were primarily directed from the center to the peripheral, i.e., target-related (Fig. 7e). Active target-related saccades may interfere with GO recognition, partially explaining the longer RTs observed in the moving condition (Fig. 1g).

Intriguingly, PreGO ICMS significantly increased the probability of saccades around GO in the moving condition, but not in the static condition (Fig. 7f). Additionally, cosθ was also more positive in ST trials of the moving condition, suggesting that ICMS induced saccade away from the periphery. In contrast, no such difference was observed in the static condition (Fig. 7g, Supplementary Fig. 17). Previous studies have shown that ICMS can evoke sensations in non-sensory areas[62–64] and even instruct specific actions in premotor cortex[65]. Further, integrating multiple sensory cues enhances perceptual sensitivity[66], and combining ICMS with weak visual signals improves target estimation[67]. Given its influence on saccade, we propose that ICMS serves as an auxiliary cue to facilitate movement initiation when preparatory activity is intact and rapid GO recognition is crucial.

Discussion

Despite that cortical control of movement has undergone conceptual shifts from representational to dynamical systems view over the decades[3,5,68], how neural dynamics adapt to dynamic environment or perturbations is not yet thoroughly understood. In this study, we investigate the intriguing effect of ICMS on an interceptive reaching task, proposing that continuous sensorimotor transformation may enhance the robustness of motor cortex against ICMS perturbations. Monkeys exhibited similar reach trajectories towards both the static (center-out task) and the moving targets (interception task) (Fig. 1). However, ICMS applied during the late delay period selectively prolonged reaction times for reaching static targets, but not moving targets (Fig. 2). Post-ICMS neural states deviated more significantly from intact states in the static condition (Fig. 3). Representations of target or reach direction for the moving targets adapted continuously with target motion throughout the delay period (Figs. 4, 5). We adapted a neural network model to illustrate optimal feedback inputs from other brain regions can efficiently mitigate perturbations-induced errors, thereby restoring RTs in the moving condition (Fig. 6). Ultimately, we propose that, in the absence of disturbances, PreGO ICMS may act as a go signal that accelerates movement onset during delayed-instructed interception (Fig. 7).

The RT-prolonging ICMS effect observed in center-out task supports the hypothesis that the brain detects errors and delays movement until they can be corrected[11,69]. Our study provides direct evidence for this hypothesis by showing that ICMS in the static condition caused neural states to deviate, requiring time to recover. Surprisingly, however, ICMS did not disrupt reach accuracy or increase RTs in interception task. Interestingly, a similar ICMS-resilient effect was noted in a previous study: ICMS to supplementary motor area (SMA) during interceptive reaches to outward-moving targets resulted in a smaller RT increase[15]. However, this study did not fully explain this ICMS effect (Supplementary Fig. 18). Our findings suggest a plausible mechanism aligned with the optimal-subspace hypothesis, indicating that disrupting activity while it is still variable has minimal impact[11]. Our results show that the moving target induced continuous sensorimotor transformation in motor cortex, manifesting as varied neural dynamics throughout the delay period. However, contrary to the mechanism suggested by the hypothesis that perturbation merely shifts the system between non-optimal states[11], we observed less post-ICMS deviation and faster recovery of neural states in the moving condition, suggesting quicker error resolution. Thus, our study provides an alternative explanation for ICMS resilience: continuously evolving preparatory neural states operate as part of an optimal feedback controller, akin to a bicycle maintaining stability while in motion, naturally resisting disturbance.

Our findings reveal significant differences in preparatory neural dynamics between the static and moving conditions, despite similar reach kinematics. Consistent with previous studies[13,14,70], we observed partial overlap in preparatory space across contexts (Supplementary Fig. 19), indicating that shared traits and unique features coexist. ICMS effect could be similar across contexts, suggesting that perturbation might impact these shared neural dynamics[15], while our results show that distinct perturbation responses can arise from different dynamics. Recent progress has unveiled a sensory-motor network that is more integrated than previously recognized[71–73]. Our recent study also suggests that stimulus motion features influence neural dynamics during interception[23]. Time-varying inputs from thalamus to motor cortex are essential for movement generation[33,35]. Optimal input-driven neural dynamics generate multiple preparation phases, relying on inputs that precede movement in reach sequences[36]. These studies highlight the importance of considering influence of external inputs on cortical dynamics for accurate interpretation of intrinsic neural behaviors[74] and causal inferences[75]. One limitation of our study is the relatively small size of the recorded neuronal population, which may influence the interpretation of subtle differences in neural dynamics, such as tortuosity in neural trajectories. However, bootstrapping analyses demonstrate that our findings are robust to variations in the number of neurons recorded (Supplementary Fig. 12).

Recent advances in modeling have reshaped our understanding of motor preparation[35,36]. By simulating the motor cortex as a self-contained dynamical system, a recent study effectively explained the differing responses to optogenetics and ICMS[42]. In the present study, we adapted a well-established neural network model with assumptions based on empirical observations to illustrate the hypothesis that different external input control strategies lead to distinct preparatory dynamics and behavioral responses to perturbation. While our model's performance aligns with the study by Kao et al.[35], our study additionally demonstrates that feedback control is essential for accurate interception and replicating key features of its preparatory activity. Furthermore, given that feedforward control was not considered as the true mechanism for motor preparation in Kao et al.'s work, it is intriguing to identify a connection between this strategy and the stationary late-delay neural dynamics in the static condition. While our model has limitations—such as ignoring circuit architecture and simplifying perturbation assumptions, which may overlook the nonlinearity of real neural networks—we extend Kao et al.'s framework and encourage further investigation through direct measurement of external input[12,14,32,70] or the development of more refined models[36,76,77].

Although the finding that PreGO ICMS reduced RTs in the moving condition is not the primary focus of our work, we offer a plausible explanation: ICMS disrupts motor preparation equally in the static and moving conditions, but it also provides information about go cue timing. Given the robustness against perturbations conferred by varying neural dynamics and the stricter timing requirements in the moving condition, monkeys may utilize the informative ICMS cue to reduce their RTs compared to the static condition. RTs in interception were longer in our study compared to center-out reach, which contrasts with previous studies that did not include a delay period[13,15,16,40,41]. The precise time-to-contact required for interception may create a conflict between estimating target motion and go cue, potentially delaying movement onset[78–80]. Given the interconnected fronto-parietal circuit[81,82] and the remote effects of ICMS[83–85], our results suggest that ICMS might serve as an implicit cue to facilitate go cue recognition. Alternative explanations, such as the StartReact effect[86] and GABAergic inhibition[87], remain possible. However, no single mechanism fully accounts for the differential ICMS effects observed, underscoring the need for future research using more specific perturbation tools, such as cooling[88] and optogenetics[89] to further unravel these effects.

In conclusion, our study demonstrates that continuous preparatory neural dynamics enhance the resilience of motor cortex during manual interception. This emphasizes that motor cortex dynamics arise from a sensorimotor transformation, integrating peripheral sensory inputs with contextual information from other cortical and subcortical areas. This interplay highlights how continuous growth, both in life and neural dynamics, enables individuals and systems to better adapt to and withstand external interference.

Methods

All procedures have been approved by the Biomedical Research Ethics Committee of Shanghai Institutes for Biological Sciences, Chinese Academy of Sciences, under permit number ER-SIBS-221603P (version 20160310). They comply with national and local laws and regulations in China and are in accordance with the Guide for Care and Use of Laboratory Animals of the Institute for Laboratory Animal Research. The details of the experimental procedures are as follows.

Experimental model

This study involved three adult male rhesus monkeys (*Macaca mulatta*): monkey G (8.4 kg, 13 years old) and monkey L (10.0 kg, 6 years old) were used for the primary analysis of the results presented in the main manuscript. Monkey D (9.0 kg, 7 years old), data from which is included in the Supplementary information, was introduced for additional analysis. Each monkey was implanted with head fixation posts and an acrylic recording chamber (19 mm inner diameter), which was secured with dental acrylic resin and titanium screws. The chambers were positioned over the upper limb areas of the primary motor cortex (M1) and the dorsal premotor cortex (PMd) in the right hemisphere for monkey G, the left hemisphere for monkey L and monkey D.

Task design and apparatus

In the manual delayed interception task[16], a head-fixed monkey was seated in a custom primate chair facing a vertical touchscreen. The arm contralateral to the chamber was free to move, while the ipsilateral arm was restrained by a shutter board (Supplementary Fig. 1a). The task began with the monkey touching the central target for 600 ms. Subsequently, a peripheral target appeared (target on, TO), which either remained static (i.e., center-out task) or moved in a fixed-radius circular path at specified velocities. Following a delay period, the central target disappeared (Go cue, GO), and the monkey was required to reach the peripheral target within 800 ms. If the touchpoint was within the error tolerance and the target is held for more than 600 ms, the touchpoint turns red, indicating a successful trial, and the monkey received one drop of liquid food as a reward; otherwise, the touchpoint turned blue (failed trial). Moving target velocities were customized for each monkey, including clockwise (-) or counterclockwise (+) 120°/s, 180°/s and 240°/s, i.e., ±120°/s, ±180°/s, ±240°/s. The delay period ranged from 0 to 1000 ms, and initial target locations varied from 0 to 360°. These parameters were randomly assigned for each trial to ensure variability.

Task control and data acquisition were managed via MonkeyLogic[90] [https://monkeylogic.nimh.nih.gov/index.html], which logged touch interactions and target locations. Reach movements were tracked using a Vicon motion capture system (Oxford, UK) equipped with MX3+ cameras that captured the trajectory of an infrared reflective marker attached to the monkey's free-moving hand at 100 Hz. Additionally, eye movements were recorded with an Eyelink infrared camera at 1000 Hz, and electromyograms (EMGs) were collected in some sessions using Delsys wireless sensors on the triceps, forearm lateral muscle, or forearm interior muscle at a sampling rate of 1259 Hz.

ICMS task design

Experiments were conducted in a single session per monkey per day, with two monkeys participating either on the same day or on alternating days. For ICMS experiments, each session contains static and one moving target velocity condition. Two delay periods were selected: 200 ms (short) and 900 ms (long). To ensure a uniform distribution of touch points across the four screen quadrants, the initial target locations were carefully selected to align with the individual reaction times and delay periods. ICMS was delivered at two timings: within 100 ms (0–100 ms) before GO (PreGO) and within 150 ms (0–150 ms) after GO (PreMO). There are three types of trials, the designed static condition, the designed moving condition, and the random condition. Designed condition trials have four initial target locations, with an equal number of condition-matched (same target velocity, initial target location, and delay period) stimulated (ST) and non-stimulated (NS) trials. Trials in the random condition are NS trials with moving targets and random initial target location. Designed ST trials were interleaved with designed NS trials and trials from the random condition. We limited the number of ST trials to be fewer than 200 per session for each recording site to protect the brain tissue. After all the designed NS and ST trials were completed, there would be 100–200 random condition trials before monkey ceasing the task naturally due to satiation. We deleted the non-stimulated trials after the last designed trial to prevent the slow drift in RTs. For monkey G, we recorded 7 sessions with target velocities of 0°/s and −120°/s, and 7 sessions at 0°/s and −240°/s. For monkey L, we recorded 12 sessions at 0°/s and −120°/s, and 3 sessions at 0°/s and 180°/s (Supplementary Tables 1 and 2).

Electrophysiological recording and ICMS parameters

In each ICMS session, we delivered stimulation using single tungsten microelectrodes (#UEWLEFSECN1E, 0.6-1.2 MΩ @1 KHz, FHC) and recorded neuronal activity with 64-channel S-probe (interelectrode spacing of 75 µm, #PLX-SP-64-15ST(100/75)-(320-140)(640-10)-570-(2) CON/32m-V, 0.3–0.5 MΩ @1 KHz, Plexon). These electrodes were advanced into the cortex through a stainless-steel guide tube using a microdrive (Thomas Motorized Electrode Manipulator), which was mounted on the recording chamber. Typically, the microelectrode and S-probe were spaced approximately 4–5 mm apart, positioned either at M1 or PMd.

Neural signals were recorded either from the microelectrode before ICMS, using an AlphaLab SnR Stimulation and Recording System (Alpha Omega) sampled at 44 kHz to confirm the presence of arm movement-related neural activity, or from the S-probe during ICMS using Cerebus acquisition system (Blackrock Microsystems) sampled at 30 kHz. To determine the depth of the recording site, the depth where the first neural activity was observed was set as the zero point, with subsequent depths relative to this. Spike sorting was performed semi-automatically using Spike2 (Spike2 7.15, CED) and Wave_clus[91].

ICMS was delivered using an AlphaLab SnR Stimulation and Recording System (Alpha Omega). Each ICMS consisted of a 100-ms train of biphasic pulses (300 Hz, 200 µs per phase, with cathode leading). To determine the amplitude threshold of each site, the monkey was instructed to keep his hand on the center of the screen to receive reward. Stimulation amplitude was increased from 30 µA in 10 µA increments until a muscle twitch or forelimb displacement was detected, either visually or palpably, or until a maximum of 120 µA was reached. Subsequently, the amplitude was reduced in 5 µA decrements until no muscle twitch or movement was detected. In this study, ICMS amplitudes remained 5–10 µA below the threshold.

Behavioral analysis

Hand velocities were derived from recorded 3D reach trajectory sampled at 100 Hz. Movement onset (MO) time was determined by identifying the time of peak hand speed and tracing it back until the speed dropped below 5% of the peak. Using this MO time as a reference, we computed the reaction time (RT, from GO to MO), movement time (MT, from movement onset to screen touch), and RT + MT.

Endpoint errors were defined as the distances between the reach endpoint and the target. Reach endpoints were monitored by a touchscreen via MonkeyLogic, and 95% covariance ellipses were computed relative to the final target location.

Reach trajectories were projected into 2D in the vertical space. Confidence intervals for the reach trajectory were calculated using Teetool [https://github.com/WillemEerland/teetool] developed by Eerland et al. (2017)[92], which models the 2D trajectories as a Gaussian process and produces an area encompassing the 1σ covariance around the mean path. To facilitate trajectory comparison, reach trajectories were rotated to align the head to the origin and the tail with 45°, 135°, 225°, and 315°.

To account for trial number imbalances and to prevent bias, we computed the difference (Δ) between stimulated (ST) trials and condition-matched non-stimulated (NS) trials. Specifically, each ST trial was paired with condition-equivalent NS trials within the same session, sharing identical delay duration, target velocities, and initial target position (±10°). The median of kinematic parameters (e.g., RTs) from the matched NS trials was subtracted from each ST trial and the corresponding NS trial within the paired group (Fig. 2, and Supplementary Fig. 3, 4).

Neural data processing and PETH

For neural data involving ICMS, we restricted our analyses to times outside the ICMS period to avoid large ICMS artifacts that could confound neural sorting results. For each trial, we identified the start and end of ICMS, and set the neural data within this range to either infinite or zero. When averaging neural data without aligning to the end of ICMS, we identified the earliest start and latest end times of ICMS across trials. This period was defined as the ICMS window for the averaged data. Consequently, data within this window were excluded from the analysis (Fig. 3).

To assess post-ICMS responses, we computed the difference between stimulated (ST) and equivalent non-stimulated (NS) trials. We randomly sampled from the ICMS onset time distribution of a specific condition to simulate the ICMS onset for the condition-equivalent NS trials. Subsequently, we aligned both ST and NS trials to the ICMS onset time and subtracted the average firing rates of equivalent NS trials from those of ST trials. Units were sorted based on mean firing rates within a 100-ms window following the cessation of the ICMS train (Fig. 3a).

Normalized firing rates heatmaps were used to assess overall neural activity. Neural activity in 20-ms bin without overlap or smoothing, in long delay condition was aligned to GO (GO − 1200ms to GO + 700 ms), averaged across all other conditions, and normalized to a mean of 0 and a standard deviation of 1. Units were sorted based on the timing of maximum firing rates (Fig. 4a).

Peri-event time histograms (PETHs) and corresponding spike rasters were used to estimate mean firing rates (FRs) over time. Spike trains were aligned to GO, binned into 10-ms window, and smoothed with a 50-ms standard deviation Gaussian filter. Trials were averaged according to conditions, such as target velocities and reach directions. Differences in FRs between conditions (e.g., static vs. moving) were evaluated using the Wilcoxon rank-sum test at each timepoint (Fig. 4b).

Histogram of time bins of firing rates discriminating between reach directions

To estimate when the firing rates show discrimination of reach directions, we conducted Kruskal–Wallis test ($p < 0.05$) for each 50-ms epoch window of condition-averaged PETH (GO − 1000 ms to GO + 600 ms) for each unit. Then, the number of significant time bins was summed across units with a bin width 55 ms. The difference between the static and moving conditions was assessed using Fisher's exact test ($p < 0.05$). Only units with mean firing rates greater than 5 sp/s around GO were selected for computation (Fig. 4c).

Bootstrap principal component analysis (PCA) with confidence intervals

Principal component analysis (PCA) is a dimensionality reduction method that identifies the primary directions of variance in a multidimensional dataset. To estimate confidence intervals for PCA components, we applied a bootstrap resampling procedure to the dataset. We first computed a reference PCA on the mean time-series data for the static NS condition, extracting the principal components (PCs) that serve as the reference structure. Specifically, neural data were initially binned at 2-ms without overlap and smoothed using a 25-ms Gaussian kernel. Subsequently, trial-averaged firing rates were organized into a neural matrix $\mathbf{X}$ of size $n \times ct$, where n is the number of recorded neurons, c is the number of conditions, and t is the number of time points. PCA was then performed on the neural matrix of static NS condition, $\mathbf{X}_{\mathrm{ref}}$ The new representations of $\mathbf{X}_{\mathrm{ref}}$ in the low-dimensional subspace were computed as $\mathbf{Y}_{\mathrm{ref}} = \mathbf{W}_{\mathrm{ref}}^{\mathrm{T}}(\mathbf{X}_{\mathrm{ref}} - \bar{\mathbf{X}}_{\mathrm{ref}})$, where $\mathbf{Y}_{\mathrm{ref}}$ of size $k \times ct$ (with $k < n$) was the PC scores of $\mathbf{X}_{\mathrm{ref}}$, and $\mathbf{W}_{\mathrm{ref}}$ of size $k \times n$ was the reference projection matrix or loadings that transform the feature space into PC space. Next, we performed bootstrap resamples ($n = 1000$ samples) on the dataset. Each bootstrap sample was generated by randomly sampling (with replacement) the trials within each condition. For each bootstrap resample, PCA was recalculated on the resampled data from the static NS condition. This process yielded a new set of PCs and scores. To ensure alignment with the original reference PCA components, we used Procrustes alignment to align the bootstrap-derived first three PCs, $\mathbf{Y}_{\mathrm{ctrl}}$ with the reference first three PCs, $\mathbf{Y}_{\mathrm{ref}}$. This step also transformed the projection matrix, $\mathbf{W}_{\mathrm{ctrl}}$ into $\mathbf{W}_{\mathrm{aligned}}$. Then, the other conditions $\mathbf{X}_{\mathrm{new}}$ (e.g., static ST, moving NS, and moving ST) were projected into the PCA space defined by the aligned components. $\mathbf{Y}_{\mathrm{new}} = \mathbf{W}_{\mathrm{aligned}}^{\mathrm{T}}(\mathbf{X}_{\mathrm{new}} - \bar{\mathbf{X}}_{\mathrm{ctrl}})$. The scores $\mathbf{Y}_{\mathrm{new}}$ represented $\mathbf{X}_{\mathrm{new}}$ in the principal subspace. After completing all bootstrap iterations, the mean PCA scores were computed across all resamples. Confidence intervals for each PCA score were calculated using percentiles from the bootstrap distribution, specifically the 95% confidence interval (CI). This was accomplished by computing the 2.5th7.5th percentiles for each time point and dimension of the PCA space (Fig. 3b, c right).

Neural trajectories

To visualize the neural trajectories, the trial-averaged conditions were plotted in the subspace constructed using the first 3 PC scores of PCA on $\mathbf{X}_{\mathrm{ctrl}}$. For neural trajectory analysis in ICMS data, the firing rates during ICMS were set to zero for each ST trial due to the loss of spikes caused by ICMS artifacts. Next, the firing rates were aligned to GO (−1000ms + 500 ms), and averaged across reach directions. The PETH in the static NS condition was used to construct the 3D state space, into which the static ST and moving conditions were projected. A representative condition (long delay, reach to quadrant 1, PreGO ICMS from dataset G0914) was selected for demonstration, with the mean MO time labeled on the trajectories (Fig. 3b, c; Supplementary Fig. 8, 9).

For neural trajectory analysis for paired static and moving condition, the firing rates were aligned to GO and averaged according to the respective conditions. An example reach direction condition (quadrant 1) was selected, with the epoch chosen for the long delay condition from GO − 1000 ms (i.e., TO − 100 ms) to GO + 500 ms (Fig. 5a).

Cross-correlation function (CCF) of PCs

To examine the post-ICMS reaction time changes embodied in neural population activity, we computed the cross-correlation function (CCF) between the population components of neural activity in non-stimulating (NS) and stimulating (ST) conditions to determine the time lag that maximizes their correlation. First, population responses of static NS, static ST, moving NS, and moving ST conditions were acquired by projecting trial-averaged (of each reach direction) neural activity (2-ms bins with 25-ms Gaussian kernel smoothing, GO − 1000 ms to GO + 600 ms) into the state space built from the static NS neural activity using PCA. Next, as the largest response component reflects movement timing[93], the last 200 ms of the first principal components (PCs) of ST and matched-NS trials were selected to calculate the normalized cross-correlation coefficient using MATLAB's xcorr function. xcorr computes the normalized cross-correlation coefficient ccf(τ) for each time lag τ of the PCs of NS, $\mathbf{x}$ and ST conditions, $\mathbf{y}$, as follows:

$$\mathrm{ccf}(\tau) = \frac{E[(\mathrm{x}(t) - \bar{x})(\mathrm{y}(t+\tau) - \bar{\mathrm{y}})]}{\sigma_x \sigma_y} \tag{3}$$

where E is the expectation, $\bar{\mathrm{x}}$ and $\bar{\mathrm{y}}$ are the means of $\mathbf{x}$ and $\mathbf{y}$, respectively, and σ_x and σ_y are their standard deviations. The optimal temporal shift, denoted as τ_{optimal}, was determined as the time lag corresponding to the maximum cross-correlation. In our case, positive τ_{optimal} indicates a lag of neural states of ST condition compared to NS condition, while negative values indicate a lead of ST condition. By identifying the τ_{optimal} for each reach condition in each session, we were able to quantify the temporal relationship between the neural states of NS and ST conditions, allowing for the estimation of RT changes post-ICMS (Fig. 3d, e).

Unbiased neural state distance

To measure the distance or difference between two multivariate distributions, such as mean firing rates in an unbiased way, we adopted cvVectorStats [https://github.com/fwillett/cvVectorStats], developed by Willett et al. (2020)[49]. This technique estimates the difference in sample means $\hat{\mathbf{u}}_d$ of the multivariate vector of trial i for distribution 1 ($\mathbf{x}_i^1$), and distribution 2 ($\mathbf{x}_i^2$) with minimal biases in a cross-validation approach:

$$\hat{\mathbf{u}}_d = \frac{1}{\mathrm{N}} \sum_{i=1}^{N} \hat{\mathbf{u}}_{d,i} \cdot \hat{\mathbf{u}}_{d,\{1:N\}/i} \tag{4}$$

where $\hat{\mathbf{u}}_{d,\{1:N\}/i}$ is the sample estimate of the difference in means using all trials except trial i.

Neural state distance is the distance between the full-dimensional PCA neural states of stimulating (ST) and matched non-stimulating (NS) condition. Here, we first built the neural state space from trial-averaged static NS condition, and projected the neural activity of each trial into the state space to obtain single-trial neural states (2-ms bins with 25-ms Gaussian kernel smoothing), thus generating, for both NS and ST conditions, for each reach direction and each session, an $t \times m \times n$ neural state matrix, where t is the number of time bin (MO − 1000 ms + 600 ms), m is the number of trials, and n is the number of neurons in each session. For each timepointunbiased Euclidean distances were computed for two distributions: $\mathbf{x}_{NS}$ with size $m_{NS} \times$ n and $\mathbf{x}_{ST}$ with size $m_{ST} \times n$. Then, single-trial neural distances were aligned to end of ICMS and averaged across reach directions and sessions. Data from ICMS end − 600 ms to + 300 ms were shown. For monkey G, 7 sessions of −120°/s target velocity with PreGO ICMS and 6 sessions of −240°/s target velocity with PreMO ICMS (totaling $13 \times 4 = 52$ samples) were averaged together, while for monkey L, 12 sessions of -120°/s target velocity with PreMO ICMS and 3 sessions of +180°/s target velocity with PreGO ICMS (totaling $15 \times 4 = 60$ samples) were averaged together (Fig. 3f).

Neural state speed

We computed the neural state speed using the neural states obtained from PCA. Specifically, similar to the processes described in Unbiased neural state distance, single-trial neural states of each condition were derived. The neural states aligned to MO were organized into a neural state matrix of size $t \times m \times k$ for each condition, where t is the number of time bin (MO − 1000 ms + 600 ms), m is the number of trials, k is the number of PCs that capture >90% of the variance ($k < n$, where n is the number of neurons per session). Next, the rate of change and the Euclidean norm of the neural states were computed to derive an overall neural speed matrix of size $(t-1) \times m$. Then, the data were aligned to the end of ICMS and averaged across reach directions and sessions, which resulted in aomparison between the static and moving conditions within either the NS or ST condition (Fig. 3g).

Targeted dimensionality reduction (TDR)

In the manuscript, we used a simplified version of targeted dimensionality reduction (TDR), firstly introduced by Mante et al.[50] and later simplified by Sun et al.[51] to identify low dimensional subspaces capturing variance related to the behavioral variables of interest. Specifically, to construct the TDR space, multivariable linear regression was used to determine how various behavioral variables affected the responses of each unit. The neural data, in 100-ms bin without overlap or smoothing, were first averaged across all trials for each condition. The activity of each neuron was then centered by subtracting its mean response at each time point for each condition. The centered responses of neuron i were a linear combination of several behavioral variables:

$$\mathrm{r_i}(k) = \beta_{i,0} + \beta_{i,x}\mathbf{L}_x(k) + \beta_{i,y}\mathbf{L}_y(k) \tag{5}$$

where $\mathrm{r}_i(k)$ is the centered trial-averaged response of unit i on condition k, averaged over a certain time window. $\mathbf{L}_x(k)$ and $\mathbf{L}_y(k)$ are the trial-averaged horizontal and vertical instantaneous target location or hand locations for condition k. The regression coefficient $\beta_{i,0}$ captures the variance independent of the listed behavioral and task variables. To estimate the regression coefficients, we constructed the behavior variable matrix $\mathbf{M}$ with dimensions conditions × regressors ($\mathbf{M} = [\mathbf{X}|1]$, $\mathbf{X} \in \mathrm{R}^{k \times 2}$), and neural activity matrix $\mathbf{R}$ with size conditions × neurons. The regression coefficients were estimated as:

$$[\boldsymbol{\beta}_0 \boldsymbol{\beta}_x \boldsymbol{\beta}_y]^{\mathrm{T}} = \mathbf{R}/\mathbf{M} = (\mathbf{M}^{\mathrm{T}}\mathbf{M})^{-1}\mathbf{M}^{\mathrm{T}}\mathbf{R} \tag{6}$$

The TDR axes were computed by finding the pseudoinverse of the regression coefficients. To ensure that the TDR axes are independent, they were orthogonalized using the Gram-Schmidt orthogonalization process. We then projected neural data into the regression subspace by multiplying the TDR axes by the neural data matrix $\mathbf{R}$.

The target location subspace was constructed by regressing neural activity at TO + 0.1 s against the static or moving condition's respective instantaneous target location. The hand reach location subspace was built by regressing neural activity at MO − 0.1 s against the final hand touch location for each condition. Neural activity at other time points (in 100-ms bins) aligned to TO was projected onto the 2D TDR subspace. To visualize the evolving neural state path in the target location TDR plane, the base (TO + 0.1 s) of each reach direction was set as the origin, with subsequent time points' locations computed relative to it. For the hand reach location subspace, each time point's location was computed relative to the origin of the plane. The neural states of the static condition were rotated by +180° in polar coordinates to align to the static target locations in each reach direction. Similarly, the neural states in the moving condition were rotated by the same angle. This suggests that TDR analysis captures the relationship among conditions without being informed of the true coordinates, confirming that the method is not artificial (Fig. 5b–d, Supplementary Fig. 13).

Input-driven neural network model

We adapted the stability-optimized circuits (SOC) neural network model with optimal feedback control [https://github.com/hennequin-lab/optimal-preparation] developed by Kao et al. (2021)[35] to simulate motor cortical activity.

Network dynamics

We model motor cortex as a network consisting of 100 excitatory (E) neurons and 100 inhibitory (I) neurons. The synaptic architecture, **W**, was constructed using the methodology of Hennequin et al. (2014)[57] and MATLAB codes [https://www.nature.com/articles/s41593-018-0276-0] developed by Stroud et al. (2018)[58]. Briefly, starting with a spectral abscissa of 10, a connection density of 0.1, an inhibition/excitation ratio of 3, and a learning rate of 10, we iteratively updated the inhibitory synapses of a random network to minimize a measure of robust network stability. Early stopping was implemented, halting the procedure when the spectral abscissa dropped below 0.15.

We modeled neuronal activity according to Eqs. (1, 2, 7, 8), which we integrate using the ode45 function (with default parameters) in MATLAB.

$$\bar{\mathbf{h}} = \mathbf{x}_{\mathrm{sp}} - \mathbf{W}\phi[\mathbf{x}_{\mathrm{sp}}] \tag{7}$$

$$\mathbf{h}(t) = (1, \ldots, 1)^{\mathrm{T}} \times \begin{cases} \text{if} \, t > t_{\mathrm{move}} : \alpha\left[\exp\left(-\frac{t - t_{\mathrm{move}}}{\tau_{\mathrm{decay}}}\right) - \exp\left(-\frac{t - t_{\mathrm{move}}}{\tau_{\mathrm{rise}}}\right)\right] \\ \text{otherwise} : 0 \end{cases} \tag{8}$$

where $\mathbf{x}(t) = (\mathbf{x}_{\mathrm{E}}(t)^{\mathrm{T}}, \mathbf{x}_{\mathrm{I}}(t)^{\mathrm{T}})^{\mathrm{T}}$ is the internal state, τ is the single-neuron time constant, **W** is the synaptic connectivity matrix, $\phi(\mathbf{x}) = \max(\mathbf{x}, 0)$ is a rectified-linear nonlinearity that converts internal states into firing rates, $\bar{\mathbf{h}}$ represents the baseline activity, with spontaneous firing rates $\mathbf{x}_{\mathrm{sp}} \sim \mathcal{N}(20, 2)$, $\mathrm{h}(t)$ is a condition-independent, spatially uniform, α-shaped input bump given during movement, α is adjusted such that $\mathrm{h}(t)$ reaches a maximum of 5. $\mathbf{u}(t)$ is the preparatory control input that drives the circuit into the appropriate state for each movement, and $\mathbf{y}(t)$ represents the hand position driven by the motor network ($\mathbf{u} = 0$), where $\mathbf{C} \in \mathrm{R}^{2 \times N}$ is the readout matrix. For the task, we set the delay period (or preparation time) to 700 ms, the movement time to 300 ms, the moving target velocity to −300 °/s, and the update interval for the desired state in the moving condition to 100 ms (Supplementary Fig. 15).

Initial state and readout matrix optimization

We optimized a set of twelve initial conditions $\{\mathbf{x}_k^*\}$ and the readout matrix $\mathbf{C}$ to calibrate the network for generating desired hand trajectories $\{\mathbf{y}_k^*\}$, where $k = 1, \ldots, 12$. The trajectories were straight reaches of length $d = 20$ cm from the origin (0, 0), with a bell-shaped speed profile $\mathbf{v}(t)$:

$$\mathbf{v}(t) = v_0 \left(\frac{t}{\tau_{\mathrm{reach}}}\right)^2 \exp\left[-\frac{1}{2}\left(\frac{t}{\tau_{\mathrm{reach}}}\right)^2\right] \tag{9}$$

where v_O is adjusted to ensure that the hand reaches the target. To minimize the loss function (Eq. 6), we used the MATLAB's fminunc function with default parameters:

$$\mathcal{L}(\mathbf{C}, \{\mathbf{x}_k^*\}) = \frac{1}{12}\sum_{k=1}^{12}\left(\int_{t_{\mathrm{move}}}^{t_{\mathrm{move}}+T} \|\mathbf{y}_k(t) - \mathbf{y}_k^*(t)\|^2 dt\right) + \frac{1}{2}\|\mathbf{C}\|^2 \tag{10}$$

$\mathbf{y}$ depends on $\mathbf{C}$ and $\mathbf{x}_k^*$ through the network dynamics (Eqs. 1, 2, 7, 8).

The initial conditions $\{\mathbf{x}_k^*\}$ were assembled using the top eigenvectors of the observability Gramian from the linearized system:

$$\tau \frac{\mathrm{dx}}{dt} = \mathbf{A}\mathbf{x}(t) + \bar{\mathbf{h}} + \mathbf{h}(\mathrm{t}) + \mathbf{u}(t) \tag{11}$$

where $\mathbf{A} \triangleq \mathbf{W} - \mathrm{I}$, and $\mathbf{Q}$ satisfies

$$\mathbf{A}^{\mathrm{T}}\mathbf{Q} + \mathbf{Q}\mathbf{A} + 2\mathbf{I} = 0 \tag{12}$$

The initial conditions were generated by linearly transforming the eigenvectors with $\mathbf{Q} \times \mathbf{x}_k^*$, and normalizing to meet a norm constraint. $\mathbf{C}$ was parameterized to ensure that no muscle output during spontaneous activity: $\mathbf{C}\phi[\mathbf{x}_{\mathrm{sp}}] = \mathbf{C}\mathbf{x}_{\mathrm{sp}} = 0$, and $\mathbf{C}(\mathbf{x}_{\mathrm{sp}} + \mathbf{x}_{\mathrm{k}}^*) = 0$.

Control cost function and classical LQR solution

We defined our total control cost functional as:

$$\mathcal{L}[\mathbf{u}(t)] = \int_0^\infty (\mathbf{C}(\mathbf{x}(t)) + \lambda R(\mathbf{u}(t)))dt \tag{13}$$

where $\mathbf{C}(\mathbf{x}(t)$ is the prospective motor error, i.e., the movement error that would result if movement was initiated at time t; $R(\mathbf{u}(t)))$ is an energetic cost penalizing large control signals; λ determines the weight of this energetic cost ($\lambda = 0.1$). The cost functional can be specified as:

$$\mathcal{L}[\mathbf{u}(t)] = \int_0^\infty \frac{dt}{\tau}[\delta\mathbf{x}(t)^{\mathrm{T}}\mathbf{Q}\delta\mathbf{x}(t) + \lambda\|\delta\mathbf{u}(t)\|^2] \tag{14}$$

where $\delta\mathbf{x}(t) \triangleq \mathrm{x}(t) - \mathbf{x}^*$, and $\delta\mathbf{u}(t) \triangleq \mathbf{u}(t) - \mathbf{u}^*$ $\mathbf{Q}$ is the observability Gramian of pair (**A, C**), satisfying the Lyapunov equation:

$$\mathbf{A}^{\mathrm{T}}\mathbf{Q} + \mathbf{Q}\mathbf{A} + \mathbf{C}^{\mathrm{T}}\mathbf{C} = 0 \tag{15}$$

The optimal control input is given by the linear quadratic regulator (LQR):

$$\mathbf{u}_{\mathrm{opt}}(t) = \mathbf{u}^* + \delta\mathbf{u}_{\mathrm{opt}}(t) = \mathbf{u}^* + \mathbf{K}\delta\mathbf{x}(t), \mathbf{K} = -\lambda^{-1}\mathbf{P} \tag{16}$$

$$\mathbf{u}^* = -\mathbf{A}\mathbf{x}^* - \bar{\mathbf{h}} \tag{17}$$

Where $\mathbf{P}$ is the solution to the Riccati equation:

$$\mathbf{A}^{\mathrm{T}}\mathbf{P} + \mathbf{P}\mathbf{A} - \lambda^{-1}\mathbf{P}\mathbf{P} + \mathbf{Q} = 0 \tag{18}$$

Perturbation simulation

To simulate the ICMS effect, we applied a perturbation input $\mathbf{h}_{\mathrm{pt}}$ to a randomly subset of neurons ($N_{\mathrm{pt}} = 100$) for 100 ms, starting 200 ms before movement onset. This timing allowed for partial error correction before movement onset. The perturbation amplitudes (0, 20, 40, or 50) were selected to reflect the response differences between the static and moving conditions. During this simulation, the input energy penalty λ was set to 1 to distinguish the effects of the two conditions.

Eye movements recording and analysis

In earlier ICMS experiments with monkey G (Supplementary Table 3), eye movements were recorded at 1000 Hz using EyeLink system (SR Research; EyeLink1000), which uses noninvasive infrared eye-tracking. An infrared mirror positioned at a 45° angle allowed eye tracking while monkey could still see the stimulus. Eye tracker calibration involved projecting a target sphere onto a 3 × 3 grid at the screen center, with the monkey required to fixate for a random interval of 100–400 ms. Calibration offsets were determined by the target sphere, and voltage changes between targets provided the scaling factor to convert eye-tracker voltage to screen distance[94].

To determine the reaction times (RTs) of eye movement, we first applied a low-pass filter (<50 Hz) to smooth out noise in the eye-velocity signal. The first and second highest peaks in the filtered velocity signal were then identified. The peak selected as the saccade onset had to meet these criteria: (1) it must occur after GO − 200ms; (2) if one peak occurs before and one after GO, the later peak is chosen; (3) if both peaks occur before or after the GO, the peak closest to GO is selected. This ensures that eye movement onset is as late as possible after GO. The relative time of this peak to GO was recorded as the RT. Trials with delay period >800 ms and target velocity of −120°/s across 35 sessions were analyzed (Fig. 7b).

To compute saccade probability, we identified peaks in the filtered eye speed signal. The five highest peaks meeting the threshold criteria (300–1000°/s) were selected. Trials with delay period > 800 ms and target velocity of ±120°/s across 35 sessions were analyzed. Saccades within specific epochs were used to calculate normalized probability: from GO − 0.9 s to GO + 0.1 s between the static vs. moving conditions, and from GO − 0.1 s to GO + 0.1 s between NS vs. ST trials. For each histogram bin, we constructed a contingency table and applied a one-tailed Fisher's exact test (alpha = 0.05) to compare counts in a certain bin to others (Fig. 7c, f).

To calculate cosθ, we computed the cosine similarity between two vectors: the saccade direction vector, from the preceding time point to the saccade peak, and the center vector, from the saccade peak to the origin. A cosθ close to +1 indicates that a centripetal saccade toward the center, whereas values close to −1 suggests a centrifugal saccade toward the peripheral (Fig. 7e, g).

Reporting summary

Further information on research design is available in the Nature Portfolio Reporting Summary linked to this article.

Data availability

The dataset generated in this study has been deposited in the Zenodo at https://zenodo.org/records/14196227 (https://doi.org/10.5281/zenodo.14196227). Source data are provided with this paper.

Code availability

Code for reproducing figures and statistics is available at https://github.com/zhengcong26/Interception_ICMS[95].

References

1. Isaacson, W. *Einstein: His Life and Universe* (Simon and Schuster, 2008).
2. Buzsaki, G. *The Brain from Inside Out* (Oxford University Press, USA, 2019).
3. Vyas, S., Golub, M. D., Sussillo, D. & Shenoy, K. V. Computation through neural population dynamics. *Annu. Rev. Neurosci.* **43**, 249–275 (2020).

4. Churchland, M. M., Cunningham, J. P., Kaufman, M. T., Ryu, S. I. & Shenoy, K. V. Cortical preparatory activity: representation of movement or first cog in a dynamical machine? *Neuron* **68**, 387–400 (2010).
5. Churchland, M. M. & Shenoy, K. V. Preparatory activity and the expansive null-space. *Nat. Rev. Neurosci*. https://doi.org/10.1038/s41583-024-00796-z (2024).
6. Shenoy, K. V., Sahani, M. & Churchland, M. M. Cortical control of arm movements: a dynamical systems perspective. *Annu. Rev. Neurosci.* **36**, 337–359 (2013).
7. Churchland, M. M. et al. Neural population dynamics during reaching. *Nature* **487**, 51–56 (2012).
8. Sussillo, D., Churchland, M. M., Kaufman, M. T. & Shenoy, K. V. A neural network that finds a naturalistic solution for the production of muscle activity. *Nat. Neurosci.* **18**, 1025–1033 (2015).
9. Pandarinath, C. et al. High performance communication by people with paralysis using an intracortical brain-computer interface. *Elife* **6**, e18554 (2017).
10. Kuzmina, E., Kriukov, D. & Lebedev, M. Neuronal travelling waves explain rotational dynamics in experimental datasets and modelling. *Sci. Rep.* **14**, 1–15 (2024).
11. Churchland, M. M. & Shenoy, K. V. Delay of movement caused by disruption of cortical preparatory activity. *J. Neurophysiol.* **97**, 348–359 (2007).
12. Ames, K. C., Ryu, S. I. & Shenoy, K. V. Neural dynamics of reaching following incorrect or absent motor preparation. *Neuron* **81**, 438–451 (2014).
13. Lara, A. H., Elsayed, G. F., Zimnik, A. J., Cunningham, J. P. & Churchland, M. M. Conservation of preparatory neural events in monkey motor cortex regardless of how movement is initiated. *Elife* **7**, 1–34 (2018).
14. Zimnik, A. J. & Churchland, M. M. Independent generation of sequence elements by motor cortex. *Nat. Neurosci.* **24**, 412–424 (2021).
15. Zimnik, A. J., Lara, A. H. & Churchland, M. M. Perturbation of macaque supplementary motor area produces context-independent changes in the probability of movement initiation. *J. Neurosci.* **39**, 3217–3233 (2019).
16. Li, Y., Wang, Y. & Cui, H. Eye-hand coordination during flexible manual interception of an abruptly appearing, moving target. *J. Neurophysiol.* **119**, 221–234 (2017).
17. Merchant, H. & Georgopoulos, A. P. Neurophysiology of perceptual and motor aspects of interception. *J. Neurophysiol.* **95**, 1–13 (2006).
18. Brenner, E. & Smeets, J. B. J. Hitting moving targets: co-operative control of 'when' and 'where'. *Hum. Mov. Sci.* **15**, 39–53 (1996).
19. Port, N. L., Lee, D., Dassonville, P. & Georgopoulos, A. P. Manual interception of moving targets. I. Performance and movement initiation. *Exp. Brain Res.* **116**, 406–420 (1997).
20. Lee, D., Port, N. L. & Georgopoulos, A. P. Manual interception of moving targets. II. On-line control of overlapping submovements. *Exp. Brain Res.* **116**, 421–433 (1997).
21. Brenner, E. & Smeets, J. B. J. Continuously updating one's predictions underlies successful interception. *J. Neurophysiol.* **120**, 3257–3274 (2018).
22. Fiehler, K., Brenner, E. & Spering, M. Prediction in goal-directed action. *J. Vis.* **19**, 1–21 (2019).
23. Zhang, Y., Chen, Y., Wang, T. & Cui, H. Neural geometry from mixed sensorimotor selectivity for predictive sensorimotor control. *Elife 2023.* **04**, 535795 (2024).
24. Bosco, G., Carrozzo, M. & Lacquaniti, F. Contributions of the human temporoparietal junction and MT/V5+ to the timing of interception revealed by transcranial magnetic stimulation. *J. Neurosci.* **28**, 12071–12084 (2008).
25. Desmurget, M. et al. Role of the posterior parietal cortex in updating reaching movements to a visual target. *Nat. Neurosci.* **2**, 563–567 (1999).
26. Li, Y., Wang, Y. & Cui, H. Posterior parietal cortex predicts upcoming movement in dynamic sensorimotor control. *Proc. Natl Acad. Sci. USA* **119**, 1–9 (2022).
27. Merchant, H., Battaglia-Mayer, A. & Georgopoulos, A. P. Neural responses during interception of real and apparent circularly moving stimuli in motor cortex and area 7a. *Cereb. Cortex* **14**, 314–331 (2004).
28. Merchant, H., Battaglia-Mayer, A. & Georgopoulos, A. P. Neural responses in motor cortex and area 7a to real and apparent motion. *Exp. Brain Res.* **154**, 291–307 (2004).
29. Lee, D., Port, N. L., Kruse, W. & Georgopoulos, A. P. Neuronal clusters in the primate motor cortex during interception of moving targets. *J. Cogn. Neurosci.* **13**, 319–331 (2001).
30. Lee, D., Port, N. L. & Georgopoulos, A. P. Manual interception of moving targets. *Exp. Brain Res.* **116**, 421–433 (1997).
31. Port, N. L. et al. Motor cortical activity during interception of moving targets. *J. Cogn. Neurosci.* **13**, 306–318 (2001).
32. Kalidindi, H. T. et al. Rotational dynamics in motor cortex are consistent with a feedback controller. *Elife* **10**, 1–3 (2021).
33. Sauerbrei, B. A. et al. Cortical pattern generation during dexterous movement is input-driven. *Nature* **577**, 386–391 (2020).
34. Vahidi, P., Sani, O. G. & Shanechi, M. M. Modeling and dissociation of intrinsic and input-driven neural population dynamics underlying behavior. *Proc. Natl. Acad. Sci. USA* **121**, e2212887121 (2024).
35. Kao, T. C., Sadabadi, M. S. & Hennequin, G. Optimal anticipatory control as a theory of motor preparation: a thalamo-cortical circuit model. *Neuron* **109**, 1567–1581.e12 (2021).
36. Schimel, M., Kao, T.-C. & Hennequin, G. When and why does motor preparation arise in recurrent neural network models of motor control? *Elife* **12**, RP89131 (2024).
37. Churchland, M. M., Yu, B. M., Ryu, S. I., Santhanam, G. & Shenoy, K. V. Neural variability in premotor cortex provides a signature of motor preparation. *J. Neurosci.* **26**, 3697–3712 (2006).
38. Rosenbaum, D. A. Human movement initiation: specification of arm, direction, and extent. *J. Exp. Psychol. Gen.* **109**, 444 (1980).
39. Riehle, A. & Requin, J. Monkey primary motor and premotor cortex: single-cell activity related to prior information about direction and extent of an intended movement. *J. Neurophysiol.* **61**, 534–549 (1989).
40. Perfiliev, S., Isa, T., Johnels, B., Steg, G. & Wessberg, J. Reflexive limb selection and control of reach direction to moving targets in cats, monkeys, and humans. *J. Neurophysiol.* **104**, 2423–2432 (2010).
41. Wong, A. L., Goldsmith, J., Forrence, A. D., Haith, A. M. & Krakauer, J. W. Reaction times can reflect habits rather than computations. *Elife* **6**, 1–18 (2017).
42. O'Shea, D. J. et al. Direct neural perturbations reveal a dynamical mechanism for robust computation. Preprint at *bioRxiv* https://doi.org/10.1101/2022.12.16.520768 (2022).
43. Thura, D. & Cisek, P. Microstimulation of dorsal premotor and primary motor cortex delays the volitional commitment to an action choice. *J. Neurophysiol.* **123**, 927–935 (2020).
44. Cisek, P. & Kalaska, J. F. Neural correlates of reaching decisions in dorsal premotor cortex: Specification of multiple direction choices and final selection of action. *Neuron* **45**, 801–814 (2005).
45. Yun, R., Mishler, J. H., Perlmutter, S. I., Rao, R. P. N. & Fetz, E. E. Responses of cortical neurons to intracortical microstimulation in awake primates. *eNeuro* **10**, 1–15 (2023).
46. Hao, Y., Riehle, A. & Brochier, T. G. Mapping horizontal spread of activity in monkey motor cortex using single pulse microstimulation. *Front. Neural Circuits* **10**, 104 (2016).

47. Afshar, A. et al. Single-trial neural correlates of arm movement preparation. *Neuron* **71**, 555–564 (2011).
48. Michaels, J. A., Dann, B., Intveld, R. W. & Scherberger, H. Predicting reaction time from the neural state space of the premotor and parietal grasping network. *J. Neurosci.* **35**, 11415–11432 (2015).
49. Willett, F. R. et al. Hand knob area of premotor cortex represents the whole body in a compositional way. *Cell* **181**, 396–409.e26 (2020).
50. Mante, V., Sussillo, D., Shenoy, K. V. & Newsome, W. T. Context-dependent computation by recurrent dynamics in prefrontal cortex. *Nature* **503**, 78–84 (2013).
51. Sun, X. et al. Cortical preparatory activity indexes learned motor memories. *Nature* **602**, 274–279 (2022).
52. Kimmel, D. L., Elsayed, G. F., Cunningham, J. P. & Newsome, W. T. Value and choice as separable and stable representations in orbitofrontal cortex. *Nat. Commun.* **11**, 3466 (2020).
53. Li, N., Daie, K., Svoboda, K. & Druckmann, S. Robust neuronal dynamics in premotor cortex during motor planning. *Nature* **532**, 459–464 (2016).
54. Cisek, P. & Kalaska, J. F. Neural mechanisms for interacting with a world full of action choices. *Annu. Rev. Neurosci.* **33**, 269–298 (2010).
55. Cisek, P. Cortical mechanisms of action selection: The affordance competition hypothesis. *Philos. Trans. R. Soc. B Biol. Sci.* **362**, 1585–1599 (2007).
56. Andersen, R. A. & Cui, H. Intention, action planning, and decision making in parietal-frontal circuits. *Neuron* **63**, 568–583 (2009).
57. Hennequin, G., Vogels, T. P. & Gerstner, W. Optimal control of transient dynamics in balanced networks supports generation of complex movements. *Neuron* **82**, 1394–1406 (2014).
58. Stroud, J. P., Porter, M. A., Hennequin, G. & Vogels, T. P. Motor primitives in space and time via targeted gain modulation in cortical networks. *Nat. Neurosci.* **21**, 1774–1783 (2018).
59. Spering, M., Schütz, A. C., Braun, D. I. & Gegenfurtner, K. R. Keep your eyes on the ball: Smooth pursuit eye movements enhance prediction of visual motion. *J. Neurophysiol.* **105**, 1756–1767 (2011).
60. Fooken, J., Yeo, S. H., Pai, D. K. & Spering, M. Eye movement accuracy determines natural interception strategies. *J. Vis.* **16**, 1–15 (2016).
61. Marinovic, W., Plooy, A. M. & Tresilian, J. R. The utilisation of visual information in the control of rapid interceptive actions. *Exp. Psychol.* **56**, 265–273 (2009).
62. Penfield, W. & Boldrey, E. Somatic motor and sensory representation in man. *Brain* **389**, 443 (1937).
63. Fried, I. et al. Functional organization of human supplementary motor cortex studies by electrical stimulation. *J. Neurosci.* **11**, 3656–3666 (1991).
64. Desmurget, M. et al. Movement intention after parietal cortex stimulation in humans. *Science* **324**, 811–813 (2009).
65. Mazurek, K. A. & Schieber, M. H. Injecting instructions into premotor cortex. *Neuron* **96**, 1282–1289.e4 (2017).
66. Gu, Y., Angelaki, D. E. & DeAngelis, G. C. Neural correlates of multisensory cue integration in macaque MSTd. *Nat. Neurosci.* **11**, 1201–1210 (2008).
67. Dadarlat, M. C., O'Doherty, J. E. & Sabes, P. N. A learning-based approach to artificial sensory feedback leads to optimal integration. *Nat. Neurosci.* **18**, 138–144 (2015).
68. Wang, T., Chen, Y. & Cui, H. From parametric representation to dynamical system: shifting views of the motor cortex in motor control. *Neurosci. Bull.* **38**, 796–808 (2022).
69. Derosiere, G., Thura, D., Cisek, P. & Duque, J. Motor cortex disruption delays motor processes but not deliberation about action choices. *J. Neurophysiol.* **122**, 1566–1577 (2019).
70. Wang, T., Chen, Y., Zhang, Y. & Cui, H. Multiplicative joint coding in preparatory activity for reaching sequence in macaque motor cortex. *Nat. Commun.* **15**, 1–15 (2024).
71. Manita, S. et al. A top-down cortical circuit for accurate sensory perception. *Neuron* **86**, 1304–1316 (2015).
72. Itokazu, T. et al. Streamlined sensory motor communication through cortical reciprocal connectivity in a visually guided eye movement task. *Nat. Commun.* **9**, 338 (2018).
73. Chen, J. L., Carta, S., Soldado-Magraner, J., Schneider, B. L. & Helmchen, F. Behaviour-dependent recruitment of long-range projection neurons in somatosensory cortex. *Nature* **499**, 336–340 (2013).
74. Vahidi, P., Sani, O. G. & Shanechi, M. M. Modeling and dissociation of intrinsic and input-driven neural population dynamics underlying behavior. *Proc. Natl Acad. Sci. USA* **121**, 1–83 (2024).
75. Jazayeri, M. & Afraz, A. Navigating the neural space in search of the neural code. *Neuron* **93**, 1003–1014 (2017).
76. Yang, G. R., Joglekar, M. R., Song, H. F., Newsome, W. T. & Wang, X. J. Task representations in neural networks trained to perform many cognitive tasks. *Nat. Neurosci.* **22**, 297–306 (2019).
77. Feulner, B. et al. Small, correlated changes in synaptic connectivity may facilitate rapid motor learning. *Nat. Commun.* **13**, 1–14 (2022).
78. Chang, C. J. & Jazayeri, M. Integration of speed and time for estimating time to contact. *Proc. Natl Acad. Sci. Usa.* **115**, E2879–E2887 (2018).
79. Lee, D. N. 16 Visuo-motor coordination in space-time. In *Advances in Psychology,* vol. 1 281–295 (Elsevier, 1980).
80. Brenner, E. et al. How can people be so good at intercepting accelerating objects if they are so poor at visually judging acceleration? *Iperception*. **7**, 2041669515624317 (2016).
81. Graziano, M. S. A. A., Taylor, C. S. R. R. & Moore, T. Complex movements evoked by microstimulation of precentral cortex. *Neuron* **34**, 841–851 (2002).
82. Cisek, P. Evolution of behavioural control from chordates to primates. *Philos. Trans. R. Soc. B Biol. Sci.* **377**, 20200522 (2022).
83. Stepniewska, I., Friedman, R. M., Miller, D. J. & Kaas, J. H. Interactions within and between parallel parietal-frontal networks involved in complex motor behaviors in prosimian galagos and a squirrel monkey. *J. Neurophysiol.* **123**, 34–56 (2020).
84. Osborn, L. E. et al. Intracortical microstimulation of somatosensory cortex generates evoked responses in motor cortex. In *Proc International IEEE/EMBS Conference on Neural Engineering, CNE NER* 2021-May, 53–56 (IEE, 2021).
85. Card, N. S. & Gharbawie, O. A. Principles of intrinsic motor cortex connectivity in primates. *J. Neurosci.* **40**, 4348–4362 (2020).
86. Carlsen, A. N. & Maslovat, D. Startle and the StartReact effect: physiological mechanisms. *J. Clin. Neurophysiol.* **36**, 452–459 (2019).
87. Sawaguchi, T., Yamane, I. & Kubota, K. Application of the GABA antagonist bicuculline to the premotor cortex reduces the ability to withhold reaching movements by well-trained monkeys in visually guided reaching task. *J. Neurophysiol.* **75**, 2150–2156 (1996).
88. Takei, T., Lomber, S. G., Cook, D. J. & Scott, S. H. Transient deactivation of dorsal premotor cortex or parietal area 5 impairs feedback control of the limb in macaques. *Curr. Biol.* **31**, 1476–1487.e5 (2021).
89. O'Shea, D. J. et al. Development of an optogenetic toolkit for neural circuit dissection in squirrel monkeys. *Sci. Rep.* **8**, 1–20 (2018).
90. Hwang, J., Mitz, A. R. & Murray, E. A. NIMH MonkeyLogic: behavioral control and data acquisition in MATLAB. *J. Neurosci. Methods* **323**, 13–21 (2019).
91. Quian Quiroga, R. & Nadasdy, Z. Unsupervised spike detection and sorting with wavelets and superparamagnetic clustering. *Neural Comput.* **16**, 1661–1687 (2004).
92. Eerland, W., Box, S., Fangohr, H. & Sóbester, A. Teetool - a probabilistic trajectory analysis tool. *J. Open Res. Softw.* **5**, 14 (2017).
93. Kaufman, M. T. et al. The largest response component in the motor cortex reflects movement timing but not movement type. *eNeuro* **3**, ENEURO.0085-16.2016 (2016).

94. de Haan, M. J., Brochier, T., Grün, S., Riehle, A. & Barthélemy, F. V. Real-time visuomotor behavior and electrophysiology recording setup for use with humans and monkeys. *J. Neurophysiol.* **120**, 539–552 (2018).
95. Zheng, C. Continuous sensorimotor transformation enhances robustness of neural dynamics to perturbation in macaque motor cortex. *Interception_ICMS*. https://doi.org/10.5281/zenodo.14959105 (2025).

Acknowledgements

We are grateful to Yongxiang Xiao for invaluable discussions; to Ruichen Zheng, Tianwei Wang and Siwei Xie for surgical expertise and experiment advice; to Chao Guan and Yizhi Lu for expert veterinary care; to Tianlin Luo for preliminary works in network modeling; to Abdulraheem Nashef, Daniel J. O'Shea, and Amy Osborn for insightful advices; to Yun Chen, Chenyang Li, Joseph Malpeli, and Yiheng Zhang for helpful comments on the manuscript. This work was supported by National Key R&D Program of China (Grant 2020YFB1313402, Grant 2017YFA0701102), National Science Foundation of China (Grant 31871047, Grant 31671075), Shanghai Municipal Science and Technology Major Project (Grant 2021SHZDZX), granted to H.C., and Shanghai Postdoc Fellowship Funding (Y95CN51621) granted to C.Z.

Author contributions

C.Z. and H.C. conceived and designed the experiments. C.Z. and Q.W. performed the experiments. C.Z. analyzed data. C.Z. wrote the paper with inputs from all authors.

Competing interests

The authors declare no competing interests.

Additional information

Supplementary information The online version contains supplementary material available at https://doi.org/10.1038/s41467-025-58421-1.

Correspondence and requests for materials should be addressed to Cong Zheng or He Cui.

Peer review information *Nature Communications* thanks Nicolas Meirhaeghe, Daniel O'Shea and the other, anonymous, reviewer(s) for their contribution to the peer review of this work. A peer review file is available.